Isogeometric Finite Volume Method for Linear Elasticity

Ameer Marzok[†§*a], Emad Shakur[†b]

[a]*The Stephen B. Klein Faculty of Aerospace Engineering, Technion - Israel Institute of Technology, Haifa, 3200003, Israel*
[b]*Department of Civil and Environmental Engineering, Technion - Israel Institute of Technology, Haifa, 3200003, Israel*

Abstract

This paper extends a recently developed isogeometric finite volume method by the authors for modeling physical problems using the finite volume method and isogeometric analysis. The concept is extended here to three-dimensional elasticity. A spatial discretization scheme is presented, in which two meshes are considered: a primary mesh and a dual mesh. The primary mesh is used for spatial discretization and geometry representation. It relies on non-uniform rational B-Splines, ensuring compatibility with computer aided design models and enabling high-order, high-continuity approximations of the primary solution field. The dual mesh is employed to define the control volumes where the governing equations are enforced in the form of integral balance equations. An intersection-based approach is adopted to define the location and construction of the control volumes. The proposed formulation guarantees both local and global conservation properties. The method is validated through several benchmark problems in two- and three-dimensional elasticity, demonstrating promising results, even in the presence of complex curved boundaries.

Keywords: Finite volume method, Isogeometric analysis, Spline-based representation, Elasticity, Curved domains

1. Introduction

Numerical models for continuum mechanics primarily rely on two families of methods: the finite volume method (FVM) and the finite element method (FEM). The former is

[†]These authors contributed equally to this work.
[§]Neubauer Assistant Professor.
[*]Corresponding author. Email: marzok@technion.ac.il

predominantly used in computational fluid dynamics (CFD), while the latter is mainly applied in solid mechanics [Idelsohn and Onate, 1994].

The use of the FVM in the CFD community originated as an extension of the classical finite difference method, in which the domain and equations are discretized in their strong form. The key difference is that FVM performs the discretization on the integral form of the governing equations, rather than on their original differential form [Patankar and Spalding, 1972; McDonald, 1971].

In contrast, the FEM gained widespread adoption in the solid mechanics community due to its close connection to the stiffness method and variational principles. Its popularity is also supported by several advantages, including its ability to handle complex geometries with ease [Zienkiewicz et al., 2013].

Derived from the integral form of the governing equations in their strong form, the FVM possesses both local and global conservation properties. This feature is particularly appealing in fluid dynamics. In contrast, the FEM, in its classical form, satisfies the governing equations in a weighted average sense; therefore, local conservation is generally not ensured.

Since the late 1980s, researchers have begun developing models for structural solid mechanics using the FVM [Demirdzic et al., 1988; Demirdžić and Martinović, 1993]. The motivations for this direction were diverse and included investigating the impact of local conservation [Vinokur, 1989], comparing results with the FEM [Fryer et al., 1991], developing unified frameworks for fluid–structure interaction [Demirdžić and Muzaferija, 1995], leveraging FVM's low memory requirements and parallel scalability [Cardiff and Demirdžić, 2021], and efficiency in adaptive mesh refinement [Yang et al., 2024a].

Demirdzic et al. [1988] proposed a FVM scheme for modeling the thermo-mechanical response during the welding process and demonstrated that it can accurately produce the temperature, displacement, and stress fields. Onate et al. [1994] demonstrated that the FVM can be interpreted as a special case of the FEM employing a non-Galerkin weighting scheme. Jasak and Weller [2000] proposed the application of a cell-centered FVM scheme for linear elasticity. Techniques from fluid mechanics were adopted to improve computational efficiency by leveraging appropriate iterative solvers. Cardiff et al. [2016] developed an unstructured cell-centered finite volume approach for linear elasticity and presented a block-coupled scheme for the solution of the equations, where the finite

area method was used to calculate the tangential gradients.

It has been shown that the standard vertex centered FVM formulation suffers from the same locking problem for bending dominated problems as the FEM with quadrilateral elements. This problem was addressed by incorporating rotational degrees of freedom [Wenke and Wheel, 2003] or alternatively by evaluating the strains at element centers [Suliman et al., 2014].

Although in elasticity related problems, the comparison of displacement errors (the primary variable) has shown comparable results between FEM and FVM formulations [Fryer et al., 1991; Onate et al., 1994; Bailey and Cross, 1995], the FVM has demonstrated advantages over standard FEM in terms of stresses (secondary variables) [Vaz Jr et al., 2009]. It should be noted that while stress results in FEM can be improved using special stress recovery schemes, these require additional computations and more involved post-processing procedures.

The extension of the FVM to problems in elasticity continues to attract interest to this day. Sevilla et al. [2019] developed a locking-free formulation to address the modeling of nearly incompressible materials. Jiao et al. [2023] presented the DMCDM method, in which a vertex-centered FVM scheme is defined over a standard FEM mesh, constructed systematically using standard FEM approximations. Xuan et al. [2025] developed an FVM model for two-dimensional contact problems. For a more comprehensive overview of the application of FVM in solid mechanics, the reader is referred to review articles that focus on this topic [Cardiff and Demirdžić, 2021].

One of the main advantages of the FVM is its ability to support integrated computational schemes for multiphysics problems. In such cases, it is possible to employ a unified spatial and temporal discretization structure across different governing equations, leveraging the local conservation property when needed. In addition, since the FVM facilitates the development of computational schemes suitable for large-scale problems through efficient parallelization, it becomes an attractive formulation for problems that inherently require a large number of degrees of freedom. Considering these advantages, various methods have been developed for fluid–structure interaction [Papadakis, 2008; Schäfer and Teschauer, 2001; Wang et al., 2024] and integrated thermo-fluid-solid schemes [Demirdžić and Muzaferija, 1995; Yang et al., 2024b,a].

The methods described above reflect a clear trend in the research and engineering

communities toward developing integrated multiphysics formulations, in which the same discretization scheme is applied to different governing equations representing various physical phenomena, such as the coupling between pressure fields and structural displacements.

In addition to numerical and discretization coupling across physical domains, recent efforts have also aimed to bridge the gap between *computer-aided design* (CAD) and numerical modeling. Standard discretization schemes in both FEM and FVM often introduce inaccuracies between the original geometry and the discretized model, primarily due to the approximation of domain boundaries using low-continuity polynomial functions, as opposed to the smooth spline-based representations employed in CAD.

In addition, most existing finite volume-based models use C^0 continuity approximations between adjacent elements. Increasing the continuity order across elements remains challenging, even when higher-order approximations are employed. In certain problems, these issues can significantly affect the solution accuracy and the convergence rates of the method [Costa et al., 2019, 2021].

Recent efforts from the finite element community (or more generally, Galerkin-based methods) have led to the development of *isogeometric analysis* (IGA) to address these issues. The development of such models dates back to the late 1990s [Kagan et al., 1998, 2003], and the approach gained particular attention following the seminal paper by Hughes et al. [2005] and the monograph by Cottrell et al. [2009], where the method was formally named IGA. In this method, a spline-based representation is adopted for both the geometry of the problem domain and the approximation of the solution field of the primary variables. This approach eliminates inaccuracies caused by geometric inconsistencies between the CAD and analysis models. In addition, the use of spline-based representations enables the systematic and efficient implementation of higher-order approximations and continuity.

Since its introduction, the method has attracted interest across various fields, including structural analysis [Cottrell et al., 2006; Nguyen et al., 2015], two-phase flow [Gomez et al., 2010], and topology optimization [Wang et al., 2018; Shakour and Amir, 2021], to name a few.

Recently, the authors proposed a novel approach that integrates IGA with FVM for heat conduction problems, namely the Isogeometric Finite Volume Method (IGFVM) [Shakur and Marzok, 2025]. The method employs a novel spatial discretization scheme in which

a primary mesh—used both to define the geometry and to construct the approximation space—relies on spline-based representations, and a dual mesh is used to define the control volumes. The resulting formulation resembles the framework of vertex-centered finite volume schemes; however, the control volumes in this approach do not exactly align with the vertices of the primary mesh due to the use of an intersection-based construction. The approach was successfully implemented to solve heat conduction problems over a variety of two-dimensional geometries.

This paper presents an additional step toward the development of integrated numerical schemes for multiphysics problems, in which the geometry is represented consistently with CAD models. First, we extend the IGFVM to solve elasticity problems, which are characterized by multiple coupled equations for each control volume. Second, the formulation is extended to accommodate 3D domains. As in standard vertex-centered schemes, the method incorporates two meshes for discretization: a primary mesh and a dual mesh. The primary mesh is used for spatial discretization and for constructing the approximation space, utilizing a *Non-Uniform Rational B-Splines* (NURBS) representation. This mesh is referred to as the *SG-mesh*. The dual mesh, referred to as the *V-mesh*, is used to define the control volumes in which the balance equations are enforced.

The remainder of the paper is organized as follows: Section 2 presents the governing equations for elasticity considered in this work. The balance equations defined over the control volumes are provided in Section 3. An introduction to IGA and the spline functions used for spatial discretization is given in Section 4, and these are later used in Section 5, where the IGFVM approach is developed for elasticity. Section 6 presents case studies used to validate the proposed method. Finally, Section 7 concludes the paper with a discussion of the results and potential future directions.

2. Governing Equations of Linear Elasticity

This paper considers problems in linear elasticity. The behavior of these problems is governed by the following system of partial differential equations:

$$\begin{aligned} -\nabla \cdot \boldsymbol{\sigma} &= \mathbf{f} \qquad \text{in } \Omega, \\ \mathbf{u} &= \hat{\mathbf{u}} \qquad \text{on } \Gamma_u, \\ \boldsymbol{\sigma} \cdot \mathbf{n} &= \hat{\mathbf{t}} \qquad \text{on } \Gamma_t. \end{aligned} \tag{1}$$

where the problem is defined over the domain $\Omega \subset \mathbb{R}^d$, with $d \in \{2, 3\}$ denoting the spatial dimension. The boundary of the domain, denoted by $\Gamma = \Gamma_u \cup \Gamma_t$, is associated with the unit outward normal vector $\mathbf{n}$ and is partitioned into two disjoint subsets ($\Gamma_u \cap \Gamma_t = \emptyset$): Γ_u and Γ_t are the parts in which the Dirichlet and Neumann boundary conditions are prescribed, respectively. $\boldsymbol{\sigma}$ represents the Cauchy stress tensor. $\mathbf{f}$ denotes the body force per unit volume, and $\hat{\mathbf{u}}$ and $\hat{\mathbf{t}}$ correspond to the prescribed displacements and traction on Γ_u and Γ_t, respectively.

The unknown displacement field is defined by $\mathbf{u}(\mathbf{x}) \in \mathbb{R}^d$. For an isotropic linear elastic material under the assumption of infinitesimal deformations, the constitutive relation is defined by Hooke's law:

$$\boldsymbol{\sigma} = 2\mu\boldsymbol{\varepsilon} + \lambda \mathrm{tr}\,(\boldsymbol{\varepsilon})\,\mathbf{I}, \tag{2}$$

where λ and μ are the Lamé parameters, $\mathbf{I}$ is the identity tensor, and $\boldsymbol{\varepsilon}$ is the strain tensor given by

$$\boldsymbol{\varepsilon} = \frac{1}{2}\left(\nabla\mathbf{u} + \nabla\mathbf{u}^T\right). \tag{3}$$

Although the formulation assumes isotropic material behavior for the sake of clarity, it can be readily extended to anisotropic elasticity without loss of generality.

3. Finite Volume Balance Equations

This section presents the numerical formulation developed for the solution of Eq. (1) using the FVM scheme. In this framework, the computational domain is discretized into control volumes, over which the governing equilibrium equations are enforced. Let $\Omega^{cv} \subset \mathbb{R}^d$, with $d \in \{2, 3\}$, denote the control volume domain. The integral form of the

equilibrium equation over Ω^{cv} is given by

$$\int_{\Omega^{cv}} (\nabla \cdot \boldsymbol{\sigma} + \mathbf{f}) \, \mathrm{d}\Omega^{cv} = \mathbf{0}. \tag{4}$$

To avoid computing second derivatives of the displacement field $\mathbf{u}(\mathbf{x})$, which appear implicitly in the divergence of the stress tensor, the divergence theorem is applied. This theorem converts the volume integral over Ω^{cv} into a surface integral over its boundary $\Gamma^{cv} = \partial\Omega^{cv}$, relating the divergence of the stress tensor to the traction vector:

$$\int_{\Omega^{cv}} \nabla \cdot \boldsymbol{\sigma} \, \mathrm{d}\Omega^{cv} = \int_{\Gamma^{cv}} \boldsymbol{\sigma} \cdot \mathbf{n} \, \mathrm{d}\Gamma^{cv}, \tag{5}$$

$\mathbf{n}$ is the unit outward normal vector defined on the boundary Γ^{cv}, and $\boldsymbol{\sigma} \cdot \mathbf{n}$ denotes the traction vector acting on $\mathrm{d}\Gamma^{cv}$.

Substituting Eq. (5) into Eq. (4), the conservation principle becomes:

$$\int_{\Gamma^{cv}} \boldsymbol{\sigma} \cdot \mathbf{n} \, \mathrm{d}\Gamma^{cv} + \int_{\Omega^{cv}} \mathbf{f} \, \mathrm{d}\Omega^{cv} = \mathbf{0}. \tag{6}$$

To complete the formulation, suitable boundary conditions are incorporated, prescribing either the traction vector $\boldsymbol{\sigma} \cdot \mathbf{n}$ (Neumann boundary condition) or the displacement field $\mathbf{u}$ (Dirichlet boundary condition) on the respective portions of the domain boundary.

Discretizing Eq. (6) over the mesh of control volumes leads to a system of algebraic equations, whose solution approximates the displacement field governed by the strong form in Eq. (1). Additional implementation details, including the treatment of boundary conditions, the construction of a spline-based representation for both the geometry and the solution field (SG-mesh), and the generation of the corresponding control volume mesh (V-mesh), are presented in the subsequent sections.

4. Introduction to Spline-Based Representations and Isogeometric Analysis

This section briefly introduces spline-based representations and their use as basis functions in analysis following the principles of IGA. While the focus here is on essential concepts relevant to the proposed method, further details on IGA and spline-based modeling can be found in [Piegl and Tiller, 1995; Cottrell et al., 2009].

4.1. Spline-based Representation

Spline-based representations, particularly Non-Uniform Rational B-Splines (NURBS), are widely used in computer-aided design (CAD) due to their ability to model complex

geometries with high precision. In this work, NURBS are employed both for geometric representation and for constructing the basis functions used in analysis.

NURBS basis functions are defined as rational functions formed from B-spline basis functions and their associated weights. Given a set of B-spline basis functions $B_{i,p}$ of degree p, and weights w_i, the univariate NURBS basis functions are defined as

$$N_{i,p}(\xi) = \frac{B_{i,p}(\xi)\, w_i}{\sum_{j=1}^{n} B_{j,p}(\xi)\, w_j}, \tag{7}$$

where $B_{i,p}(\xi)$ is the i-th B-spline basis function of degree p, defined over the knot vector

$$\Xi = [\xi_1, \xi_2, \ldots, \xi_{n+p+1}],$$

and n is the number of control points. The weights $w_i \in \mathbb{R}$ are positive and influence the shape of the curve. The B-spline functions $B_{i,p}$ are evaluated using the Cox–de Boor recursive algorithm [Piegl and Tiller, 1995].

Univariate NURBS basis functions can be extended to higher dimensions through tensor-product constructions. For surfaces, let $B_{i,p}(\xi)$ and $B_{j,q}(\eta)$ be B-spline basis functions of degrees p and q in the parametric directions ξ and η, respectively. The corresponding bivariate NURBS basis function is defined as

$$N_{i,j}^{p,q}(\xi,\eta) = \frac{B_{i,p}(\xi)\, B_{j,q}(\eta)\, w_{i,j}}{\displaystyle\sum_{k=1}^{n_\xi}\sum_{l=1}^{n_\eta} B_{k,p}(\xi)\, B_{l,q}(\eta)\, w_{k,l}}, \tag{8}$$

where $w_{i,j}$ denotes the weight associated with the tensor-product basis function $B_{i,p}(\xi)\, B_{j,q}(\eta)$.

Similarly, the trivariate NURBS basis function for three-dimensional domains is given by

$$N_{i,j,k}^{p,q,r}(\xi,\eta,\zeta) = \frac{B_{i,p}(\xi)\, B_{j,q}(\eta)\, B_{k,r}(\zeta)\, w_{i,j,k}}{\displaystyle\sum_{l=1}^{n_\xi}\sum_{m=1}^{n_\eta}\sum_{n=1}^{n_\zeta} B_{l,p}(\xi)\, B_{m,q}(\eta)\, B_{n,r}(\zeta)\, w_{l,m,n}}, \tag{9}$$

where $w_{i,j,k}$ denotes the weight associated with the tensor-product basis function $B_{i,p}(\xi)\, B_{j,q}(\eta)\, B_{k,r}(\zeta)$.

To define NURBS-based geometries, a set of control points is introduced. Together with the NURBS basis functions, these control points define the mapping from the parametric domain to the physical domain. The geometry is represented as a linear combination of control points and their corresponding basis functions.

For a NURBS curve, the geometric mapping from the parametric to the physical space is expressed as

$$\mathbf{C}(\xi) = \sum_{i=1}^{n} N_{i,p}(\xi)\, \mathbf{P}_i, \tag{10}$$

where $\mathbf{P}_i \in \mathbb{R}^d$ are the control points defining the curve geometry in the physical domain.

Similarly, a NURBS surface is defined as

$$\mathbf{S}(\xi, \eta) = \sum_{i=1}^{n} \sum_{j=1}^{m} N_{i,j}^{p,q}(\xi, \eta)\, \mathbf{P}_{i,j}, \tag{11}$$

where $\mathbf{P}_{i,j} \in \mathbb{R}^d$ denote the control points of the surface.

For three-dimensional geometries, a NURBS volume is defined as

$$\mathbf{V}(\xi, \eta, \zeta) = \sum_{i=1}^{n} \sum_{j=1}^{m} \sum_{k=1}^{l} N_{i,j,k}^{p,q,r}(\xi, \eta, \zeta)\, \mathbf{P}_{i,j,k}, \tag{12}$$

where $\mathbf{P}_{i,j,k} \in \mathbb{R}^d$ represent the volumetric control points defining the geometry.

4.2. Isogeometric Analysis

Isogeometric analysis is a computational framework that unifies geometry representation and numerical approximation by employing the same spline-based basis functions for both. This approach eliminates geometry approximation errors, ensures high-order continuity, and can potentially reduce the number of degrees of freedom compared to traditional finite element methods. Following this concept, the NURBS basis functions introduced above are used to represent both the geometry and the solution field. Denoting the NURBS-based approximation of the displacement field by $\mathbf{u}_h$, it is expressed as

In two dimensions:

$$\mathbf{u}_h(\xi, \eta) = \sum_{i=1}^{n} \sum_{j=1}^{m} N_{i,j}^{p,q}(\xi, \eta)\, \tilde{\mathbf{u}}_{i,j}, \tag{13}$$

In three dimensions:

$$\mathbf{u}_h(\xi, \eta, \zeta) = \sum_{i=1}^{n} \sum_{j=1}^{m} \sum_{k=1}^{l} N_{i,j,k}^{p,q,r}(\xi, \eta, \zeta)\, \tilde{\mathbf{u}}_{i,j,k}, \tag{14}$$

where $\tilde{\mathbf{u}}_{i,j}$ and $\tilde{\mathbf{u}}_{i,j,k}$ denote the control point values representing the discrete displacement field. Each control point $\tilde{\mathbf{u}} \in \mathbb{R}^d$, with $d \in \{2, 3\}$ denoting the spatial dimension of the physical domain. In two dimensions, $\tilde{\mathbf{u}}_{i,j} = [\tilde{u}_{i,j}^x, \tilde{u}_{i,j}^y]$, while in three dimensions, $\tilde{\mathbf{u}}_{i,j,k} = [\tilde{u}_{i,j,k}^x, \tilde{u}_{i,j,k}^y, \tilde{u}_{i,j,k}^z]$. These control variables constitute the unknowns of the numerical formulation.

5. Isogeometric Finite Volume Method for Elasticity

In this section, the IGFVM is presented for two-dimensional and three-dimensional elasticity problems. We begin with the discretization strategy of the spline-based computational domain into control volumes. Then, we reformulate the balance equations of elasticity (see Eq. 6) in terms of an approximated solution field. Finally, we present the application of the balance equations to the mesh of control volumes, leading to the construction of the algebraic linear system. We note that the IGFVM was introduced in [Shakur and Marzok, 2025] in the context of 2D heat conduction.

5.1. discretization into control volumes

To discretize spline-based geometries into control volumes, we employ the intersection-based approach developed in [Shakur and Marzok, 2025] and extend the idea for 3D geometries. In this method, control volumes are defined as subdomains within the parametric space, each associated with a dominant basis function. Specifically, the parametric domain is partitioned such that each control volume spans the region between the intersection points of the dominant basis function with its adjacent basis functions on either side. For the first and last basis functions, where an adjacent function is absent on one side, the corresponding intersection point coincides with the boundary of the parametric domain.

This discretization yields a non-overlapping set of control volumes whose union recovers the entire domain. In addition, a full-rank algebraic system of linear equations is obtained, as the number of control points matches the number of control volumes, and the equations formulated over each control volume correspond to the degrees of freedom of its associated control point. For example, in two-dimensional problems, two balance equations for the two displacement components are formulated for each control volume.

To illustrate the discretization process, we consider the two-dimensional parametric domain shown in Figure 1. The basis functions defined over this domain are bi-cubic, with degrees $p = q = 3$, and are constructed using the knot vectors $\Xi = [0, 0, 0, 0, 1, 2, 3, 3, 3, 3]$ and $H = \Xi$. These functions are constructed using Eq. (8) by taking the tensor product of the univariate basis functions illustrated in the figure. The intersections of the basis functions are depicted by blue lines. The figure illustrates that the parametric domain is discretized into a 6×6 grid of control volumes, which corresponds to the 6×6 mesh of basis functions (or control points) used to represent the geometry.

With the control volumes defined in the parametric domain, their physical counterparts are determined via the geometric mapping to the physical domain, using Equations (10), (11), or (12). To illustrate the discretization into control volumes in the physical space, we refer to the examples shown in Figures 2 and 3 for the two-dimensional and three-dimensional cases, respectively.

In the two-dimensional case, associating the control point polygon depicted in Figure 2a with the basis functions illustrated in Figure 1 results in the spline-based surface, referred to as the SG-mesh, shown in Figure 2b. The corresponding control volume discretization of this surface, referred to as the V-mesh, is presented in Figure 2c.

In the three-dimensional case, we illustrate the finite volume discretization using the spline-based volume example shown in Figure 3. This volume is constructed with tri-quadratic spline basis functions using the following open knot vectors: $\Xi = [0, 0, 0, 1, 2, 3, 3, 3]$, $H = [0, 0, 0, 1, 2, 2, 2]$, and $Z = H$. The control mesh, the resulting spline geometry (SG-mesh), and the corresponding control volume discretization (V-mesh) are shown in Figures 3a, 3b, and 3c, respectively.

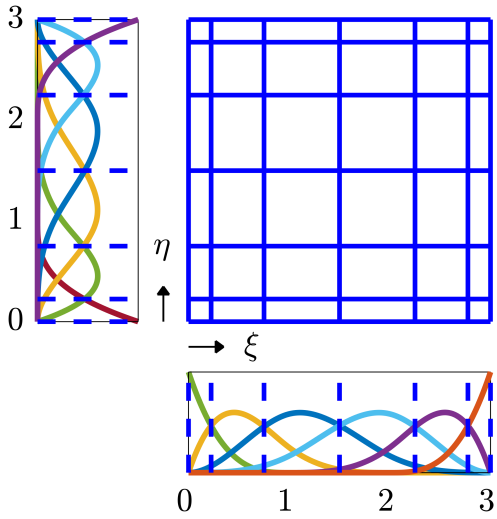

Fig. 1. Illustration of the discretization of a two-dimensional parametric domain into control volumes. The domain is defined by the knot vectors $\Xi = [0, 0, 0, 0, 1, 2, 3, 3, 3, 3]$ and $H = \Xi$. The cubic univariate basis functions used to construct the bivariate basis are shown along the bottom and left sides of the domain.

5.2. Approximation of the Solution Field

In this subsection, the balance equation, Eq. (6), is reformulated using the NURBS-based solution field. For linear elasticity, the constitutive relation given in Eq. (2) can be expressed in terms of the numerical approximation as

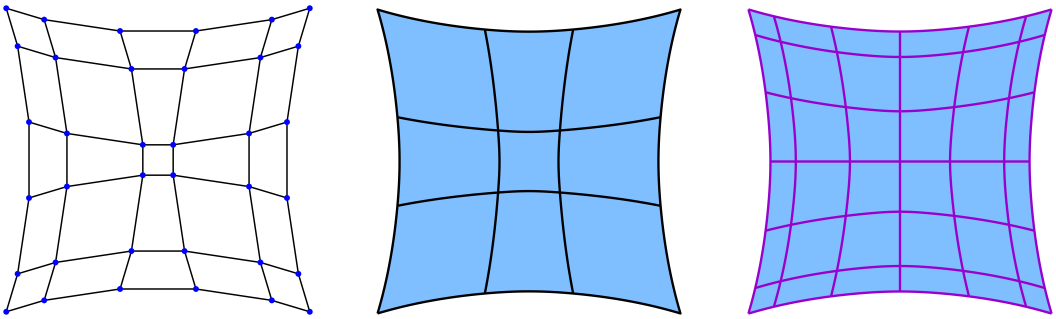

Fig. 2. A two-dimensional spline-based surface defined by bi-cubic polynomial degrees over a 6×6 mesh of control points, constructed using open knot vectors $\Xi = [0, 0, 0, 0, 1, 2, 3, 3, 3, 3]$ and $H = \Xi$. (a) Control polygon, (b) Spline geometry (SG-mesh), (c) Control volume discretization (V-mesh).

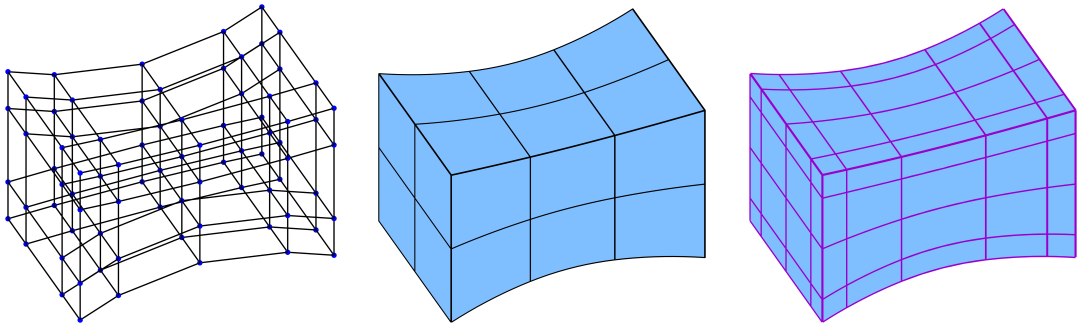

Fig. 3. A three-dimensional spline-based volume defined by tri-quadratic basis functions over a $5{\times}4{\times}4$ mesh of control points, constructed using open knot vectors $\Xi = [0, 0, 0, 1, 2, 3, 3, 3]$, $H = [0, 0, 0, 1, 2, 2, 2]$, and $Z = H$. (a) Control polygon, (b) Spline geometry (SG-mesh), (c) Control volume discretization (V-mesh).

$$\tilde{\boldsymbol{\sigma}} = \mathbf{C}\,\mathbf{B}\,\tilde{\mathbf{u}}, \tag{15}$$

where $\tilde{\boldsymbol{\sigma}}$ denotes the numerical stress vector in Voigt notation, $\mathbf{C}$ is the constitutive (material stiffness) matrix, $\mathbf{B}$ is the strain–displacement matrix derived from the spline basis functions, and $\tilde{\mathbf{u}}$ is the vector of displacement degrees of freedom. Accordingly, the numerical traction $\mathbf{t}_h$ at a given point is computed as

$$\mathbf{t}_h = \hat{\mathbf{N}}\,\tilde{\boldsymbol{\sigma}} = \hat{\mathbf{N}}\,\mathbf{C}\,\mathbf{B}\,\tilde{\mathbf{u}}, \tag{16}$$

where $\hat{\mathbf{N}}$ is a matrix that transforms the surface normal vector $\mathbf{n}$ into a form consistent with the Voigt notation of the stress tensor. This transformation encodes the directional components of $\mathbf{n}$ such that the product with $\tilde{\boldsymbol{\sigma}}$ yields the physical traction vector in the spatial coordinates. For completeness, the explicit forms of the matrices $\mathbf{C}$, $\mathbf{B}$, and $\hat{\mathbf{N}}$ are provided in Appendix A for both two- and three-dimensional cases.

Substituting Eq. (16) into the balance equation (6) yields the following expression:

$$\int_{\Gamma^{cv}} \hat{\mathbf{N}}\,\mathbf{C}\,\mathbf{B}\,\tilde{\mathbf{u}}\,\mathrm{d}\Gamma^{cv} + \int_{\Omega^{cv}} \mathbf{f}\,\mathrm{d}\Omega^{cv} = \mathbf{0}. \tag{17}$$

This expression represents the balance equations over each control volume in terms of the NURBS-based discretization. It yields d equations per control volume, where $d = 2$ for two-dimensional problems and $d = 3$ for three-dimensional problems, corresponding to the balance equations in each spatial direction. A detailed description of the numerical implementation and the assembly of the global system of equations is provided in the following subsections.

5.3. Integration over Control Volume Boundaries

In this subsection, we provide details on the numerical integration of the boundary integral in Eq. (17) over each control volume. To perform the integration, we decompose Γ^{cv} into its constituent edges (in 2D) or faces (in 3D), and apply Gaussian quadrature on each segment. Given the structured nature of the spline-based geometries considered in this work, each two-dimensional control volume consists of four edges, while each three-dimensional control volume consists of six faces. In the following, we provide further details of the integration procedure for both two- and three-dimensional cases.

*5.3.1. **Two-Dimensional Case:***

Consider a control volume defined over the parametric domain $\Omega_e = [\xi_s, \xi_e] \times [\eta_s, \eta_e]$, as illustrated in Figure 4. The parametric boundaries of the control volume are determined according to the procedure described in Section 5.1. Accordingly, the edges of Ω_e in the parametric domain are characterized by the intervals listed in Table 1.

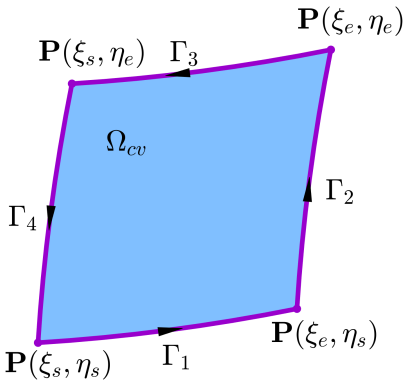

Fig. 4. A two-dimensional spline-based control volume illustrating its limits in the parametric domain (ξ, η) and its boundary edges.

Having the edges defined, the boundary integral in Eq. (17) can be evaluated as follows:

Edge	ξ Range	η Range
Γ_1	$[\xi_s, \xi_e]$	$\eta = \eta_s$
Γ_2	$\xi = \xi_e$	$[\eta_s, \eta_e]$
Γ_3	$[\xi_s, \xi_e]$	$\eta = \eta_e$
Γ_4	$\xi = \xi_s$	$[\eta_s, \eta_e]$

Table 1. Parametric definitions of the boundary edges of a two-dimensional control volume Ω_{cv}.

$$\begin{aligned}\oint_{\Gamma^{cv}} \hat{\mathbf{N}}\,\mathbf{C}\,\mathbf{B}\,\tilde{\mathbf{u}}\,\mathrm{d}\Gamma^{cv} = &\int_{\xi_s}^{\xi_e} \hat{\mathbf{N}}_{\Gamma_1}(\xi,\eta_s)\,\mathbf{C}\,\mathbf{B}(\xi,\eta_s)\,\tilde{\mathbf{u}}\,J_\xi(\xi,\eta_s)\,\mathrm{d}\xi \\ &+ \int_{\eta_s}^{\eta_e} \hat{\mathbf{N}}_{\Gamma_2}(\xi_e,\eta)\,\mathbf{C}\,\mathbf{B}(\xi_e,\eta)\,\tilde{\mathbf{u}}\,J_\eta(\xi_e,\eta)\,\mathrm{d}\eta \\ &- \int_{\xi_e}^{\xi_s} \hat{\mathbf{N}}_{\Gamma_3}(\xi,\eta_e)\,\mathbf{C}\,\mathbf{B}(\xi,\eta_e)\,\tilde{\mathbf{u}}\,J_\xi(\xi,\eta_e)\,\mathrm{d}\xi \\ &- \int_{\eta_e}^{\eta_s} \hat{\mathbf{N}}_{\Gamma_4}(\xi_s,\eta)\,\mathbf{C}\,\mathbf{B}(\xi_s,\eta)\,\tilde{\mathbf{u}}\,J_\eta(\xi_s,\eta)\,\mathrm{d}\eta. \end{aligned} \tag{18}$$

Each term corresponds to one of the four edges of the control volume. The Jacobians are defined as:

$$J_\xi = \left\|\frac{\mathrm{d}\boldsymbol{\Gamma}}{\mathrm{d}\xi}\right\| = \sqrt{\left(\frac{\mathrm{d}x}{\mathrm{d}\xi}\right)^2 + \left(\frac{\mathrm{d}y}{\mathrm{d}\xi}\right)^2}, \quad J_\eta = \left\|\frac{\mathrm{d}\boldsymbol{\Gamma}}{\mathrm{d}\eta}\right\| = \sqrt{\left(\frac{\mathrm{d}x}{\mathrm{d}\eta}\right)^2 + \left(\frac{\mathrm{d}y}{\mathrm{d}\eta}\right)^2}.$$

The negative signs in the integrals over Γ_3 and Γ_4 arise from the reversed directions of integration along the respective parametric coordinates.

5.3.2. *Three-Dimensional Case:*

Consider a control volume defined over the parametric domain $\Omega_e = [\xi_s, \xi_e]\times[\eta_s, \eta_e]\times[\zeta_s, \zeta_e]$, as illustrated in Figure 5. The six faces of Ω_e in the parametric space are characterized by the intervals listed in Table 2.

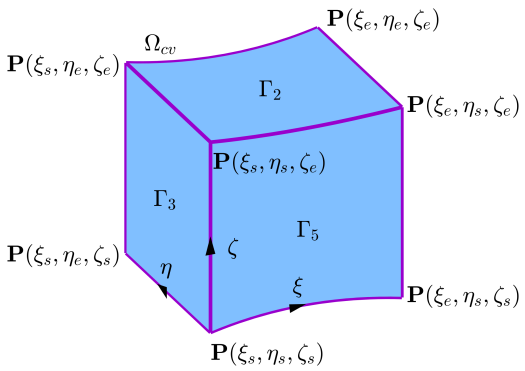

Fig. 5. A three-dimensional spline-based control volume illustrating its limits in the parametric domain (ξ,η,ζ) and its boundary faces.

Face	ξ Range	η Range	ζ Range
Γ_1	$[\xi_s, \xi_e]$	$[\eta_s, \eta_e]$	$\zeta = \zeta_s$
Γ_2	$[\xi_s, \xi_e]$	$[\eta_s, \eta_e]$	$\zeta = \zeta_e$
Γ_3	$\xi = \xi_s$	$[\eta_s, \eta_e]$	$[\zeta_s, \zeta_e]$
Γ_4	$\xi = \xi_e$	$[\eta_s, \eta_e]$	$[\zeta_s, \zeta_e]$
Γ_5	$[\xi_s, \xi_e]$	$\eta = \eta_s$	$[\zeta_s, \zeta_e]$
Γ_6	$[\xi_s, \xi_e]$	$\eta = \eta_e$	$[\zeta_s, \zeta_e]$

Table 2. The parametric ranges defining the six faces of a three-dimensional control volume $\Omega_{cv} = [\xi_s, \xi_e] \times [\eta_s, \eta_e] \times [\zeta_s, \zeta_e]$.

$$
\begin{aligned}
\oint_{\Gamma^{cv}} \hat{\mathbf{N}}\,\mathbf{C}\,\mathbf{B}\,\tilde{\mathbf{u}}\,\mathrm{d}\Gamma^{cv} = &\int_{\xi_s}^{\xi_e}\int_{\eta_s}^{\eta_e} \hat{\mathbf{N}}_{\Gamma_1}(\xi,\eta,\zeta_s)\,\mathbf{C}\,\mathbf{B}(\xi,\eta,\zeta_s)\,\tilde{\mathbf{u}}\,J_{\xi\eta}(\xi,\eta,\zeta_s)\,\mathrm{d}\eta\,\mathrm{d}\xi \\
&+ \int_{\xi_s}^{\xi_e}\int_{\eta_s}^{\eta_e} \hat{\mathbf{N}}_{\Gamma_2}(\xi,\eta,\zeta_e)\,\mathbf{C}\,\mathbf{B}(\xi,\eta,\zeta_e)\,\tilde{\mathbf{u}}\,J_{\xi\eta}(\xi,\eta,\zeta_e)\,\mathrm{d}\eta\,\mathrm{d}\xi \\
&+ \int_{\eta_s}^{\eta_e}\int_{\zeta_s}^{\zeta_e} \hat{\mathbf{N}}_{\Gamma_3}(\xi_s,\eta,\zeta)\,\mathbf{C}\,\mathbf{B}(\xi_s,\eta,\zeta)\,\tilde{\mathbf{u}}\,J_{\eta\zeta}(\xi_s,\eta,\zeta)\,\mathrm{d}\zeta\,\mathrm{d}\eta \\
&+ \int_{\eta_s}^{\eta_e}\int_{\zeta_s}^{\zeta_e} \hat{\mathbf{N}}_{\Gamma_4}(\xi_e,\eta,\zeta)\,\mathbf{C}\,\mathbf{B}(\xi_e,\eta,\zeta)\,\tilde{\mathbf{u}}\,J_{\eta\zeta}(\xi_e,\eta,\zeta)\,\mathrm{d}\zeta\,\mathrm{d}\eta \\
&+ \int_{\xi_s}^{\xi_e}\int_{\zeta_s}^{\zeta_e} \hat{\mathbf{N}}_{\Gamma_5}(\xi,\eta_s,\zeta)\,\mathbf{C}\,\mathbf{B}(\xi,\eta_s,\zeta)\,\tilde{\mathbf{u}}\,J_{\xi\zeta}(\xi,\eta_s,\zeta)\,\mathrm{d}\zeta\,\mathrm{d}\xi \\
&+ \int_{\xi_s}^{\xi_e}\int_{\zeta_s}^{\zeta_e} \hat{\mathbf{N}}_{\Gamma_6}(\xi,\eta_e,\zeta)\,\mathbf{C}\,\mathbf{B}(\xi,\eta_e,\zeta)\,\tilde{\mathbf{u}}\,J_{\xi\zeta}(\xi,\eta_e,\zeta)\,\mathrm{d}\zeta\,\mathrm{d}\xi \qquad (19)
\end{aligned}
$$

The normal vectors and Jacobian determinants in the above equation are computed as follows. For each quadrature point on a boundary face, the physical coordinates $\mathbf{x} = \mathbf{x}(\xi, \eta, \zeta)$ are first evaluated from the corresponding parametric coordinates. The partial derivatives $\frac{\partial \mathbf{x}}{\partial \xi}$, $\frac{\partial \mathbf{x}}{\partial \eta}$, and $\frac{\partial \mathbf{x}}{\partial \zeta}$ are then computed at that point. The Jacobian determinant for each face is obtained as the norm of the cross product of the two tangent vectors spanning the face:

$$
J_{\xi\eta} = \left\| \frac{\partial \mathbf{x}}{\partial \xi} \times \frac{\partial \mathbf{x}}{\partial \eta} \right\|, \quad J_{\eta\zeta} = \left\| \frac{\partial \mathbf{x}}{\partial \eta} \times \frac{\partial \mathbf{x}}{\partial \zeta} \right\|, \quad J_{\xi\zeta} = \left\| \frac{\partial \mathbf{x}}{\partial \xi} \times \frac{\partial \mathbf{x}}{\partial \zeta} \right\|.
$$

The outward-pointing unit normal vector for each face is computed by normalizing the corresponding cross product. For a given face Γ_i, spanned by the parametric directions u and v, the normal vector is given by

$$
\mathbf{n}_{\Gamma_i} = \frac{\frac{\partial \mathbf{x}}{\partial u} \times \frac{\partial \mathbf{x}}{\partial v}}{\left\| \frac{\partial \mathbf{x}}{\partial u} \times \frac{\partial \mathbf{x}}{\partial v} \right\|}.
$$

The Neumann boundary conditions are incorporated at this stage. On any edge (in

2D) or face (in 3D) where a traction is prescribed (see Eq. (1)), the integrands in Eq. (19) are modified accordingly. Assuming that the prescribed traction acts in the i-th spatial direction (with $i \in \{x, y\}$ in 2D or $i \in \{x, y, z\}$ in 3D) and is applied on the j-th boundary segment (with $j \in \{1, \ldots, 4\}$ in 2D or $j \in \{1, \ldots, 6\}$ in 3D), the corresponding boundary integral takes the form

$$\int_{\Gamma_j^{cv}} \tilde{t}_i \, \mathrm{d}\Gamma_j, \tag{20}$$

where $\tilde{t}_i$ denotes the prescribed traction component in the i-th direction on the boundary segment Γ_j^{cv}.

5.4. Assembling the System of Equations

After computing the local balance equations for all control volumes using the procedure described in the previous sections, the equations are assembled into a global system represented by the matrix $\mathbf{A}$ and the vector of unknowns $\tilde{\mathbf{u}}$. Each balance equation associated with a control volume and a spatial direction occupies one row in the global matrix. The resulting system takes the form:

$$\mathbf{A}\tilde{\mathbf{u}} = \mathbf{f},$$

where $\mathbf{f}$ contains the contributions from body forces and the prescribed tractions.

Dirichlet boundary conditions on Γ_u are imposed by splitting the global system of equations into fixed and free degrees of freedom. The resulting reduced system is solved for the unknown displacements, while the prescribed values are enforced directly at the corresponding control points; see [Shakur and Marzok, 2025].

6. Case Studies

This section presents three case studies to validate the IGFVM method. A convergence study is conducted, and the results obtained using the proposed method are compared with those from the Galerkin IGA approach, implemented following the methodology presented in [Cottrell et al., 2009]. The first two case studies address 2D and 3D problems with analytical solutions, while the third case study considers a general structural engineering shape. Refined meshes are generated using h-refinement knot insertion algorithms and p-refinement degree elevation algorithms [Piegl and Tiller, 1995; Cottrell et al., 2009].

6.1. Infinite Plate with a Hole

In this case study, the IGFVM approach is applied to the classical problem of an infinite plate with a circular hole subjected to uniform in-plane tension at infinity. An analytical solution exists for the specified boundary conditions. By utilizing the problem's double symmetry, only one-quarter of the domain is modeled, representing a finite plate of size 4×4 units with a circular hole of radius 1 unit. Appropriate boundary conditions are imposed to account for the infinite domain: symmetric conditions are applied along the two axes of symmetry, while the remaining edges are subjected to analytical tractions corresponding to a remote stress of $T_x = 10$. These analytical tractions are provided in [Gould and Feng, 1994] and considered in the model following Eq. 20. The material properties are defined by Poisson's ratio $\nu = 0.3$ and Young's modulus $E = 1$. The problem setup is illustrated in Figure 6.

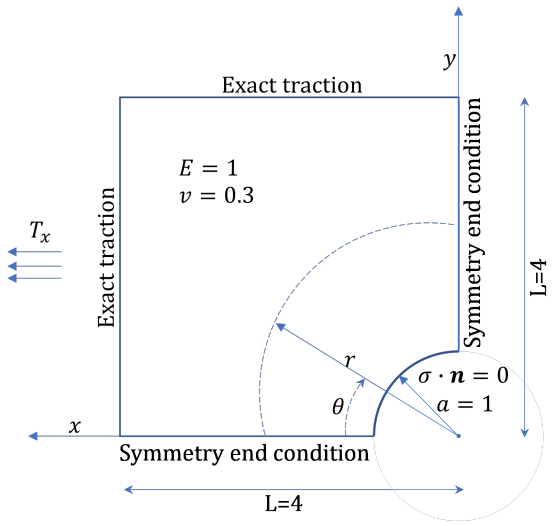

Fig. 6. Problem setting for the infinite plate with a circular hole.

Following the IGFVM approach, both the geometry of the plate and the solution field are represented using a NURBS surface, which accurately captures the geometry of the circular hole. The problem is solved for polynomial degrees $p = 2$, 3, and 4 across five levels of h-refinement. The initial NURBS representation is bi-quadratic, with control points, weights, and knot vectors obtained from [Hughes et al., 2005]. For h-refinement, we adopt the strategy proposed in [Hughes et al., 2005], which was specifically developed for this benchmark problem. According to this strategy, elements are prioritized to be split approximately in half in the physical domain, rather than uniformly in the parametric domain. For p-refinement, we apply the degree elevation algorithm described in [Piegl and Tiller, 1995]. It is important to note that we first perform p-refinement followed by h-refinement. This ordering results in C^1 continuity of the solution field along the diagonal of the model, while achieving C^{p-1} continuity along all other parts of the domain. For more details, see the k-refinement scheme in [Hughes et al., 2005].

The control polygons, NURBS geometries, and control volume discretizations corresponding to polynomial degrees $p = 2$, 3, and 4 without h-refinement are illustrated in Figure 7. The corresponding configurations with higher levels of h-refinement are shown in Figure 8. The parametric discretization of the univariate basis functions into control volumes, which forms the basis for the control volume layout shown in Figure 7, is illustrated separately in Figure 9.

To demonstrate the ability of the IGFVM to accurately capture physical quantities along curved boundaries, we present the stress field in the x-direction over the domain for $p = 2$ and three levels of h-refinement in Figure 10. Additionally, in Figure 11, we show the stress in the x-direction along the circular boundary for $p = 3$ and various levels of h-refinement. The evaluation is performed directly along the precise curved boundary. Additionally, the smoothness of the stress along the circular boundary is C^{p-2}, except at the diagonal point, where the continuity reduces to C^0 for all polynomial degrees. This localized reduction in continuity arises from the preserved knot multiplicity during p-refinement, as discussed in [Hughes et al., 2005]. The ability to evaluate stresses directly on the exact boundary is particularly useful for problems involving stress concentrations, which are highly sensitive to the geometric representation of the boundary. More generally, the capability to capture physical quantities accurately along the boundary is beneficial for other boundary-sensitive problems as well, such as two-phase flow and fluid–structure

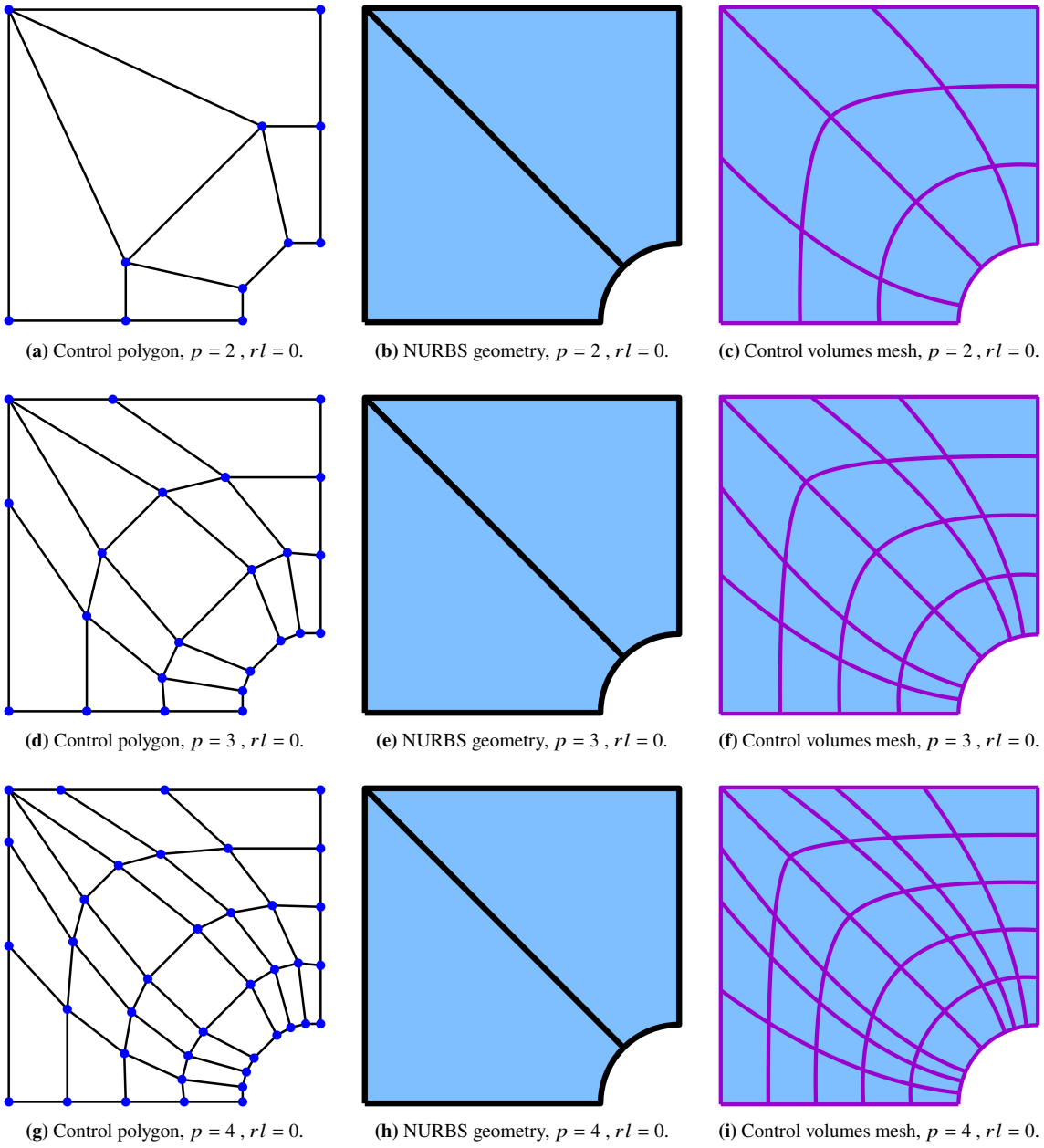

(a) Control polygon, $p = 2$, $rl = 0$. **(b)** NURBS geometry, $p = 2$, $rl = 0$. **(c)** Control volumes mesh, $p = 2$, $rl = 0$.

(d) Control polygon, $p = 3$, $rl = 0$. **(e)** NURBS geometry, $p = 3$, $rl = 0$. **(f)** Control volumes mesh, $p = 3$, $rl = 0$.

(g) Control polygon, $p = 4$, $rl = 0$. **(h)** NURBS geometry, $p = 4$, $rl = 0$. **(i)** Control volumes mesh, $p = 4$, $rl = 0$.

Fig. 7. Control polygons, NURBS geometries, and control volume discretizations for polynomial degrees $p = 2$, 3, and 4 without h-refinement for the infinite plate with a hole. The abbreviation rl denotes the refinement level.

interaction.

Figure 12 illustrates the convergence of the L^2-norm of the error in the x-direction stress component, $\|\sigma^A_{xx} - \sigma^h_{xx}\|_{L^2(\Omega)}$, with respect to the maximum element size $h_{\max}$, for polynomial degrees $p = 2$, 3, and 4. The convergence rates obtained are 1.9, 3.0, and 3.7 for $p = 2$,3, and 4, respectively. To further examine these convergence rates, we solve the same problem using Galerkin IGA, as presented in [Hughes et al., 2005], where comparable convergence rates are obtained.

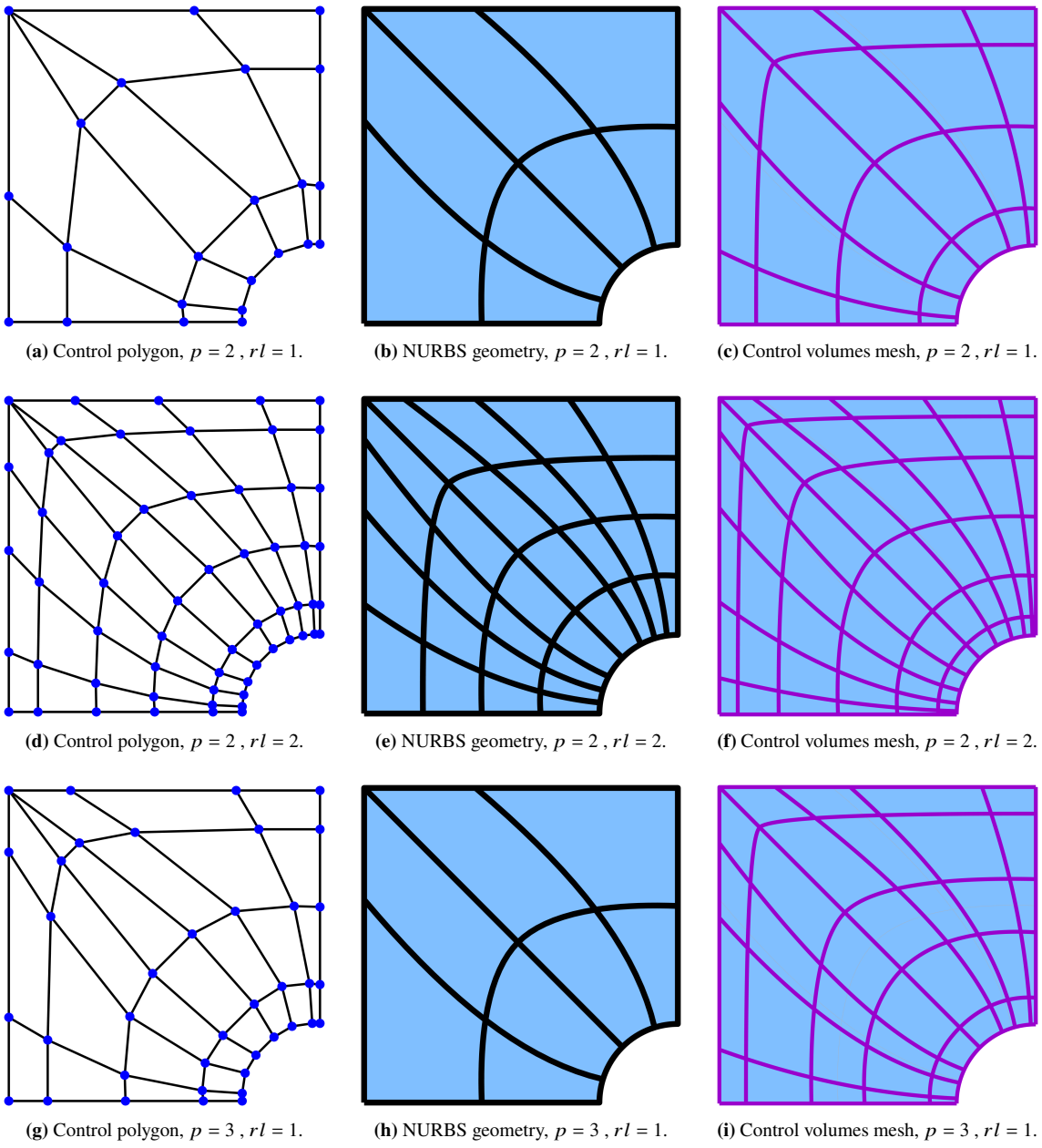

(a) Control polygon, $p = 2$, $rl = 1$. **(b)** NURBS geometry, $p = 2$, $rl = 1$. **(c)** Control volumes mesh, $p = 2$, $rl = 1$.

(d) Control polygon, $p = 2$, $rl = 2$. **(e)** NURBS geometry, $p = 2$, $rl = 2$. **(f)** Control volumes mesh, $p = 2$, $rl = 2$.

(g) Control polygon, $p = 3$, $rl = 1$. **(h)** NURBS geometry, $p = 3$, $rl = 1$. **(i)** Control volumes mesh, $p = 3$, $rl = 1$.

Fig. 8. Control polygons, NURBS geometries, and control volume discretizations for different polynomial degrees and *h*-refinement levels for the infinite plate with a hole. The abbreviation *rl* denotes the refinement level.

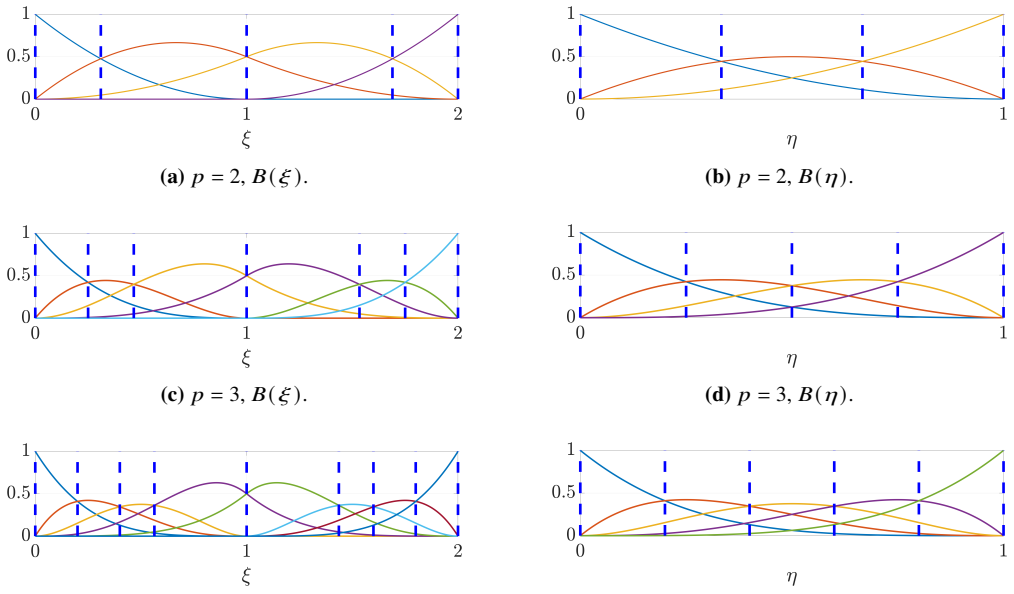

(a) $p = 2$, $B(\xi)$. **(b)** $p = 2$, $B(\eta)$.

(c) $p = 3$, $B(\xi)$. **(d)** $p = 3$, $B(\eta)$.

(e) $p = 4$, $B(\xi)$. **(f)** $p = 4$, $B(\eta)$.

Fig. 9. Univariate discretizations of the parametric domains in the ξ and η directions into control volumes for polynomial degrees $p = 2$, 3, and 4 with no h-refinement. B refers to the B-spline basis functions.

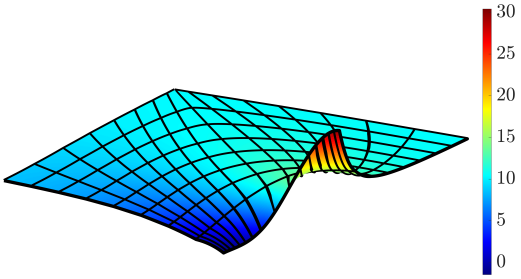

Fig. 10. Stress field in the x-direction for $p = 2$ and three levels of h-refinement ($rl = 3$) over the domain.

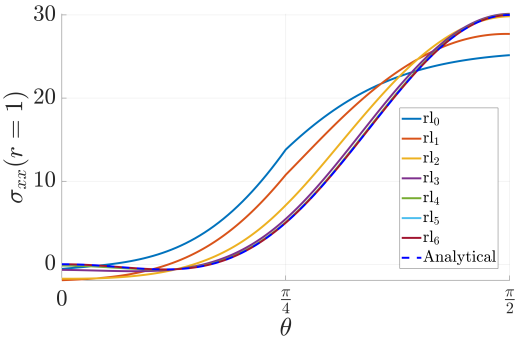

Fig. 11. Stress field in the x-direction along the circular boundary for $p = 3$ and different levels of h-refinement.

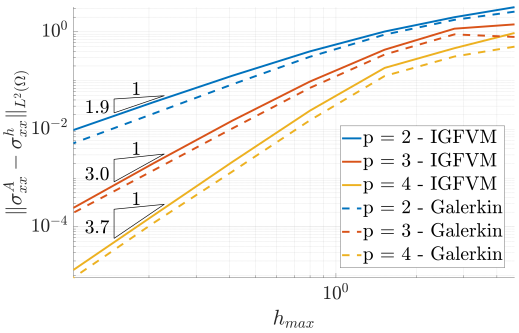

Fig. 12. Convergence of the L^2-norm of the error in the x-direction stress for different polynomial degrees for the infinite plate with a hole.

6.2. Thick-Walled Hollow Cylinder Under Internal Pressure

In this case study, we demonstrate the capability of the proposed IGFVM in a three-dimensional setting. The problem consists of a thick-walled hollow cylinder with inner and outer radii of $R_i = 1$ and $R_o = 2$, respectively, and a length $L = 5$. The cylinder is fixed at both ends and subjected to a uniform internal pressure of $P = 1$. The elasticity modulus and Poisson's ratio are taken as $E = 1$ and $\nu = 0.3$, respectively. The problem setup is illustrated in Figure 13. An analytical solution for the stress distribution is available in [Boresi and Schmidt, 2002]. Based on this solution, the analytical radial displacement can be derived under the plane strain assumption, with the detailed derivation provided in Appendix Appendix B. In the absence of external pressure the radial displacement is given by:

$$u_r = \frac{p_i R_i^2 r (1+\nu)}{E\left(R_o^2 - R_i^2\right)} \left[(1-2\nu) + \frac{R_o^2}{r^2}\right].$$

By exploiting the double symmetry of the geometry and loading, only one quarter of the cylinder is modeled, with appropriate symmetry boundary conditions applied.

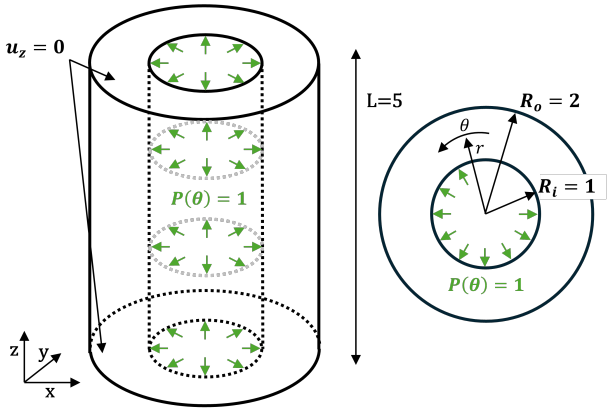

Fig. 13. Problem setup of the thick-walled hollow cylinder subjected to internal pressure.

The geometry with the coarsest mesh is represented using one element in both the longitudinal (z) and tangential (θ) directions, where the structural response is expected to remain constant, and two elements in the radial direction (r), along which variations in the structural response are anticipated. The NURBS geometry of different polynomial degrees is constructed by quarter annuli in the x-y plane of a certain degree, whose control points are given in [Shakur and Marzok, 2025], and then extruded in the z-direction to obtain the 3D geometry.

To examine convergence, the problem is solved for polynomial degrees $p = 2$, 3, and 4 across six refinement levels, starting from the coarsest mesh, defined as refinement

level 0. The control polygons, along with the NURBS geometries and the control volume discretizations for different polynomial degrees $p = 2$, 3, and 4 without h-refinement ($rl = 0$), are illustrated in Figure 14.

Figure 15 presents the radial displacement and the stress components σ_{rr} and $\sigma_{\theta\theta}$ over the geometry for a polynomial degree of $p = 2$ and one refinement level. Figure 16 depicts the percentage radial displacement error $e_u = 100\,\frac{u-u_h}{u}$ for $p = 2$ across various refinement levels. The maximum displacement errors are $1.309 \times 10^{-1}\%$, $1.658 \times 10^{-2}\%$, $1.049 \times 10^{-2}\%$, $1.109 \times 10^{-3}\%$, $9.611 \times 10^{-5}\%$, and $5.714 \times 10^{-6}\%$ for refinement levels 0 to 5, respectively. An approximately one-order-of-magnitude reduction in the percentage error is observed with each successive refinement level, demonstrating the expected convergence behavior of the method.

Figure 17 illustrates the convergence of the energy norm error given by:

$$\|e\|_E = \left(\int_\Omega (\boldsymbol{\varepsilon}_h - \boldsymbol{\varepsilon}^{\text{exact}}) : \mathbb{C} : (\boldsymbol{\varepsilon}_h - \boldsymbol{\varepsilon}^{\text{exact}})\, d\Omega \right)^{1/2},$$

shown with respect to the maximum element size $h_{r\max}$ in the radial direction for polynomial degrees $p = 2, 3$, and 4. The observed convergence rates are 1.7 for $p = 2$, 3.0 for $p = 3$, and 3.7 for $p = 4$. To further assess these rates, the same problem is solved using the Galerkin IGA approach [Hughes et al., 2005], which exhibits comparable convergence behavior. Similar rates are also obtained for the L_2 norm of the stresses in both the radial and tangential directions.

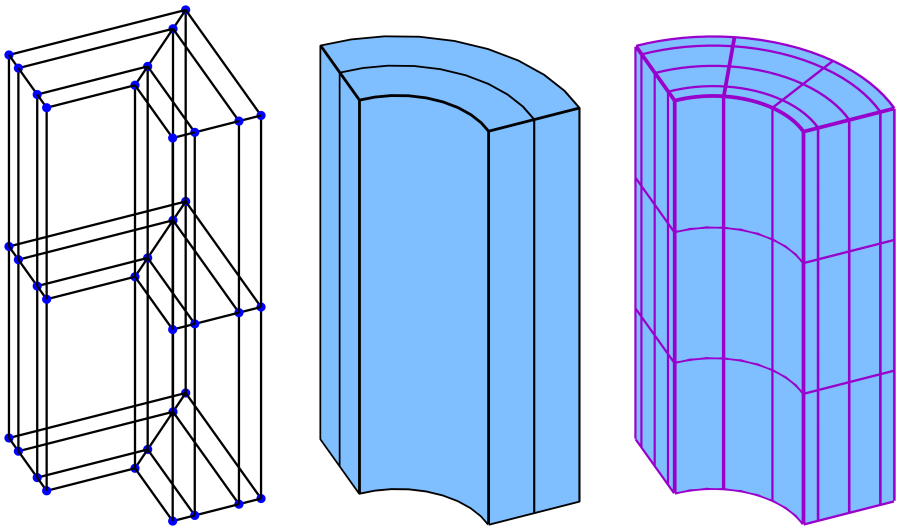

(a) Control polygon, $p = 2$, $rl = 0$.

(b) NURBS geometry, $p = 2$, $rl = 0$.

(c) Control volumes mesh, $p = 2$, $rl = 0$.

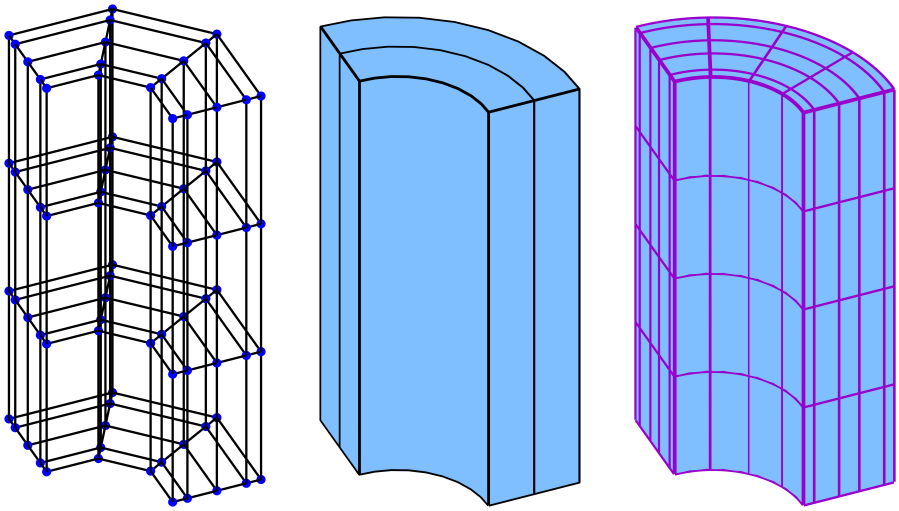

(d) Control polygon, $p = 3$, $rl = 0$.

(e) NURBS geometry, $p = 3$, $rl = 0$.

(f) Control volumes mesh, $p = 3$, $rl = 0$.

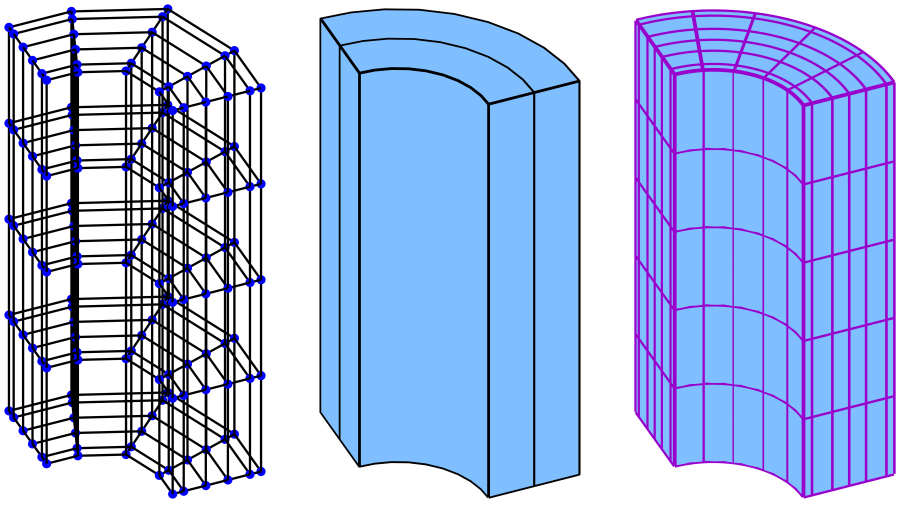

(g) Control polygon, $p = 4$, $rl = 0$.

(h) NURBS geometry, $p = 4$, $rl = 0$.

(i) Control volumes mesh, $p = 4$, $rl = 0$.

Fig. 14. Control polygons, NURBS geometries, and control volume discretizations for polynomial degrees $p = 2$, 3, and 4 without h-refinement for the hollow cylinder. The abbreviation rl denotes the refinement level.

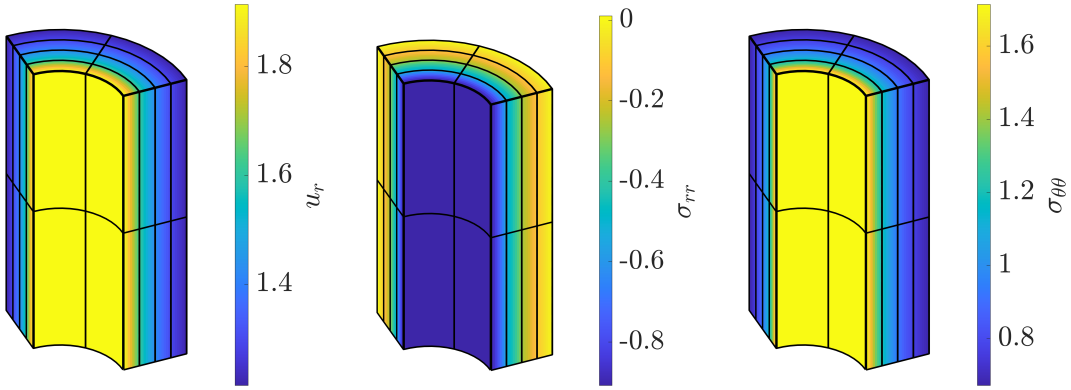

(a) u_r **(b)** σ_{rr} **(c)** $\sigma_{\theta\theta}$

Fig. 15. Radial displacement and stress components σ_{rr} and $\sigma_{\theta\theta}$ over the geometry for a polynomial degree of $p = 2$ with a single refinement level.

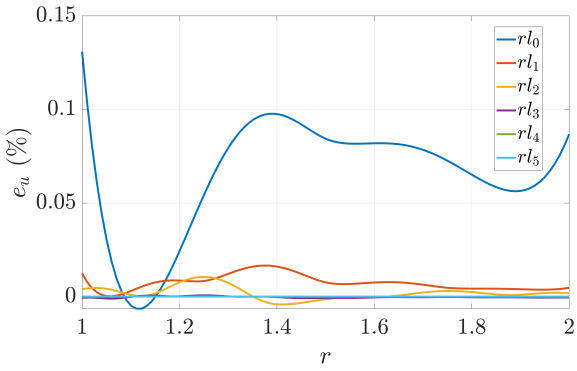

Fig. 16. Percentage radial displacement error for $p = 2$ across refinement levels 0–5.

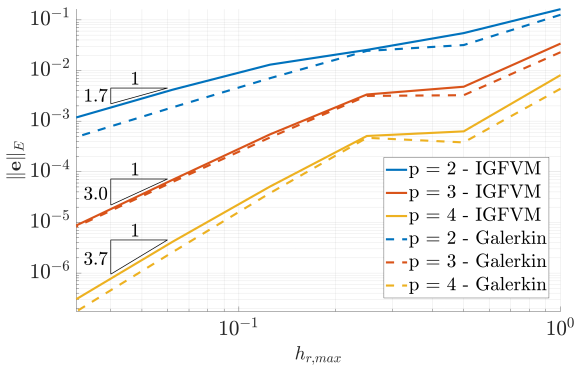

Fig. 17. Convergence of the energy norm of the error for different polynomial degrees for the thick-walled hollow cylinder under internal pressure.

6.3. Variable-Thickness Dome with Oculus

In this case study, we demonstrate the application of the IGFVM to a general curved geometry that can be represented using a structured mesh. The selected example is a three-dimensional variable-thickness dome with an oculus. The material parameters and dimensions are chosen from the field of structural engineering, allowing the geometry to represent a realistic concrete dome. To fully exploit the capability of NURBS to exactly represent conic sections (e.g., circles and ellipses) and, by extension, three-dimensional shapes such as spheres and ellipsoids, the dome is designed with a spherical outer surface of radius $r_s = 25$ m and an ellipsoidal inner surface with a vertical semi-axis $a = 25$ m and a planar semi-axis $b = 15$ m. The dome includes an oculus of radius $r_o = 7.5$ m, cut vertically through the structure. The elasticity modulus and Poisson's ratio are set to $E = 30{,}000$ MPa and $\nu = 0.2$, respectively, and the specific weight is taken as 25 kN/m^3. The dome is subjected to two loads: (i) a volume load representing the self-weight and (ii) a distributed area load of 50 kN/m^2 applied over the oculus ring. The overall problem setup is illustrated in Figure 18.

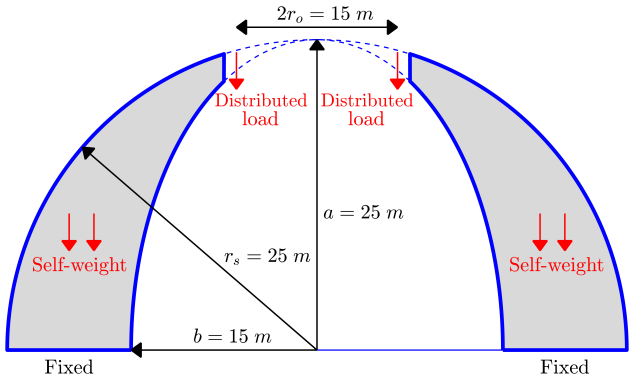

Fig. 18. Problem setup for the variable-thickness dome with an oculus.

Utilizing the double symmetry of the problem, only a quarter of the dome is modeled and analyzed. The dome model is initially represented by a single biquadratic spline-based element. The geometry is generated as follows: First, the inner and outer surfaces are defined using control points and weights corresponding to one eighth of a sphere and an ellipsoid of the given dimensions, respectively, without a hole. Knot insertion is then applied to each surface to create the circular opening of the oculus at the specified radius. An additional control polygon is inserted midway between the control polygons of the two outer surfaces, and the connectivity is completed to obtain the final dome geometry. The control points and weights of the three-dimensional geometry are provided in Table C.3 in

Appendix Appendix C. Figure 19 illustrates the control polygon, the NURBS geometry, and the control volume discretization for the single-element geometry.

To examine convergence, the vertical displacement and Von-Mises stress at the center of the oculus ring, measured across six levels of h-refinement. To avoid overly elongated elements, the analysis begins with a coarser mesh consisting of two elements in each tangential direction and one element in the radial direction. The control polygon, NURBS geometry, and control volume discretization of the initial mesh, along with its first h-refined level, are illustrated in Figure 20.

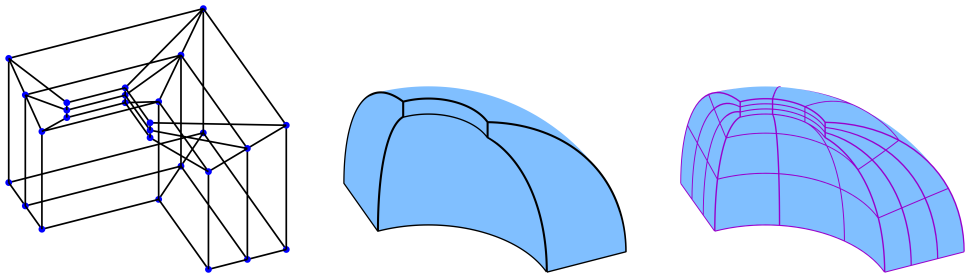

(a) Control polygon. **(b)** NURBS geometry. **(c)** Control volumes mesh.

Fig. 19. Control polygon, NURBS geometry, and control volume discretization for the variable-thickness dome with an oculus.

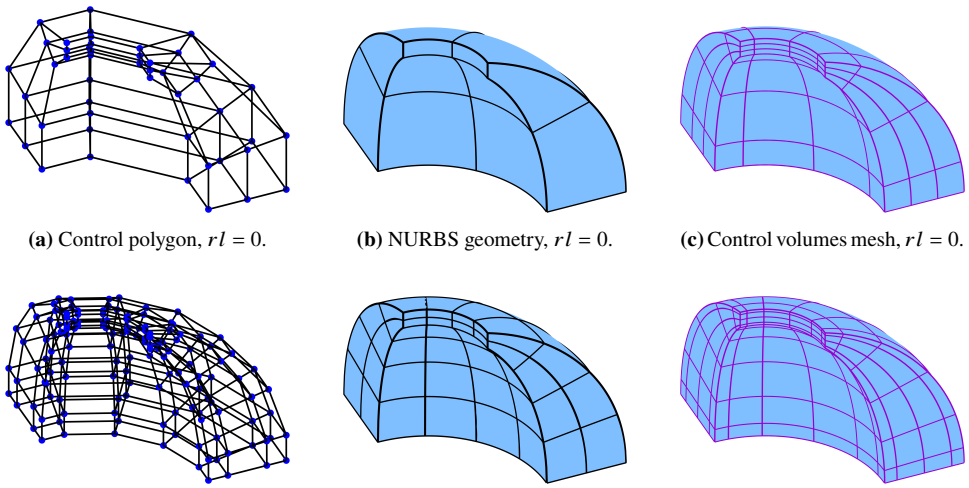

(a) Control polygon, $rl = 0$. **(b)** NURBS geometry, $rl = 0$. **(c)** Control volumes mesh, $rl = 0$.

(d) Control polygon, $rl = 1$. **(e)** NURBS geometry, $rl = 1$. **(f)** Control volumes mesh, $rl = 1$.

Fig. 20. Control polygon, NURBS geometry, and control volume discretization for the variable-thickness dome with an oculus. The first row corresponds to the coarsest mesh with zero refinement level ($rl = 0$), and the second row corresponds to the first refinement level ($rl = 1$).

Figure 21a presents the vertical displacement at the selected point as a function of the maximum radial element size of the dome across the refinement levels. The graph shows that the vertical displacement converges to a value of -0.3211 mm, with an absolute difference on the order of 0.0002 mm with a relative difference of 0.06% between the

last two mesh refinement levels. Figure 21b presents the stress obtained at the center of the oculus ring as a function of the maximum radial element size of the dome across the refinement levels. The graph shows that the stress converges to a value of 411.13 kPa, with an absolute difference on the order of 1.12 kPa with a relative difference of 0.27% between the last two mesh refinement levels. These results demonstrate that the IGFVM achieves reasonable convergence for general shapes while preserving its inherent characteristics as a control volume formulation.

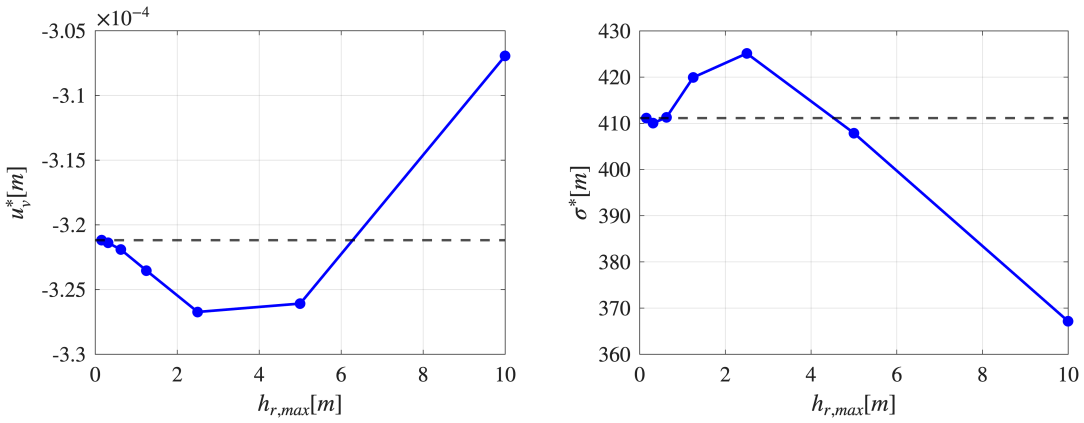

Fig. 21. Convergence of the vertical displacement and Von-Mises stress at the center of the oculus ring with respect to the maximum radial element size of the dome across successive refinement levels.

Finally, several graphs of the displacement and stress fields are presented to provide a general overview of the structural response. The von Mises stress distribution, the vertical displacement field, and the deformed shape in a perspective view are illustrated in Figure 22.

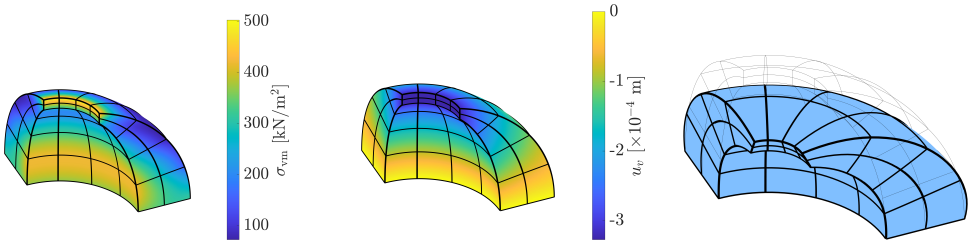

(a) Von Mises stress. **(b)** Vertical displacement. **(c)** Deformed shape (perspective view).

Fig. 22. Results for the variable-thickness dome with an oculus: (a) von Mises stress distribution, (b) vertical displacement, and (c) deformed shape in perspective view.

7. Discussion

In this paper, we have extended the Iso-Geometric Finite Volume Method (IGFVM), originally developed for two-dimensional heat conduction [Shakur and Marzok, 2025], to three-dimensional elasticity problems. This extension addresses new challenges arising from the coupling between governing equations in different spatial directions. By combining Isogeometric Analysis (IGA) with a Finite Volume Method (FVM), the approach enables the development of multiphysics models with consistent discretization and a shared mesh, ensuring accurate boundary representation and offering the potential for more efficient and versatile formulations. This represents an important step toward a unified framework for multiphysics simulations.

The proposed approach employs a geometrically consistent isogeometric framework for both the geometry description and the approximation of the primary state variables. The FVM is used to construct the balance equations over control volumes, which are defined based on the intersections of the basis functions, resulting in non-overlapping volumes and a full-rank algebraic system. This formulation ensures an accurate and consistent representation of spline-based domains commonly used in CAD systems.

The validity of the proposed method was examined through three case studies. The first case study considers a 2D domain representing an infinite plate with a circular hole, a geometry with curved boundaries. Results were compared with analytical solutions for various polynomial degrees and boundary conditions, demonstrating that the method achieves comparable convergence errors and rates to the standard Galerkin IGA approach. The second case study investigates a 3D thick-walled hollow cylinder, with results again compared to analytical solutions. Similar trends to the 2D case were observed, highlighting the method's extendability to 3D problems. The final case study addresses a practical structure, a variable-thickness dome with an oculus, featuring complex ellipsoidal and spherical boundaries. The results illustrate the robustness of the proposed approach in handling general structured geometries.

As noted, this work extends the IGFVM approach to 3D elasticity, moving toward a unified multiphysics numerical scheme. Future research will extend the formulation to multiphysics applications, aiming to investigate and demonstrate the full potential of the proposed method for such problems.

Appendix A. Explicit Matrix Definitions

2D Case: For a linear isotropic material under plane stress and plane strain conditions, the constitutive matrices $\mathbf{C}$ in Voigt notation are given respectively by:

$$\mathbf{C}_{\text{plane stress}} = \frac{E}{1-\nu^2}\begin{bmatrix} 1 & \nu & 0 \\ \nu & 1 & 0 \\ 0 & 0 & \frac{1-\nu}{2} \end{bmatrix}, \qquad \mathbf{C}_{\text{plane strain}} = \frac{E}{(1+\nu)(1-2\nu)}\begin{bmatrix} 1-\nu & \nu & 0 \\ \nu & 1-\nu & 0 \\ 0 & 0 & \frac{1-2\nu}{2} \end{bmatrix}$$

where E is Young's modulus and ν is Poisson's ratio.

The strain-displacement matrix $\mathbf{B}$ at a given point is defined as:

$$\mathbf{B} = \begin{bmatrix} \frac{\partial N_1}{\partial x} & 0 & \cdots & \frac{\partial N_n}{\partial x} & 0 \\ 0 & \frac{\partial N_1}{\partial y} & \cdots & 0 & \frac{\partial N_n}{\partial y} \\ \frac{\partial N_1}{\partial y} & \frac{\partial N_1}{\partial x} & \cdots & \frac{\partial N_n}{\partial y} & \frac{\partial N_n}{\partial x} \end{bmatrix}, \tag{A.1}$$

where N_i are the NURBS basis functions, and n denotes the number of non-zero basis functions at the evaluation point. The size of $\mathbf{B}$ is $3 \times 2n$, corresponding to the three strain components in two dimensions and the $2n$ displacement degrees of freedom. For a spline surface of bi-degree p and q in its parametric directions, the number of non-zero basis functions is $n = (p+1)(q+1)$.

Traction Transformation Matrix in 2D: To compute the traction vector $\boldsymbol{t} = \boldsymbol{\sigma} \cdot \mathbf{n}$ from the stress vector $\tilde{\boldsymbol{\sigma}}$ expressed in Voigt notation, we introduce a transformation matrix $\hat{\mathbf{N}} \in \mathbb{R}^{2\times 3}$ such that

$$\tilde{\boldsymbol{\sigma}} = \begin{bmatrix} \sigma_{xx} \\ \sigma_{yy} \\ \sigma_{xy} \end{bmatrix}, \quad \mathbf{n} = \begin{bmatrix} n_x \\ n_y \end{bmatrix}, \quad \boldsymbol{t} = \hat{\mathbf{N}}\,\tilde{\boldsymbol{\sigma}}.$$

The matrix $\hat{\mathbf{N}}$ is defined as

$$\hat{\mathbf{N}} = \begin{bmatrix} n_x & 0 & n_y \\ 0 & n_y & n_x \end{bmatrix}.$$

This transformation enables expressing the traction vector in terms of the displacement degrees of freedom as

$$\boldsymbol{t} = \boldsymbol{\sigma} \cdot \mathbf{n} = \hat{\mathbf{N}}\,\tilde{\boldsymbol{\sigma}} = \hat{\mathbf{N}}\,\mathbf{C}\,\mathbf{B}\,\tilde{\mathbf{u}}.$$

3D Case: For a linear isotropic material in three dimensions, the constitutive matrix $\mathbf{C}$ in Voigt notation is given by:

$$\mathbf{C} = \frac{E}{(1+\nu)(1-2\nu)} \begin{bmatrix} 1-\nu & \nu & \nu & 0 & 0 & 0 \\ \nu & 1-\nu & \nu & 0 & 0 & 0 \\ \nu & \nu & 1-\nu & 0 & 0 & 0 \\ 0 & 0 & 0 & \frac{1-2\nu}{2} & 0 & 0 \\ 0 & 0 & 0 & 0 & \frac{1-2\nu}{2} & 0 \\ 0 & 0 & 0 & 0 & 0 & \frac{1-2\nu}{2} \end{bmatrix} \tag{A.2}$$

The strain-displacement matrix $\mathbf{B}$ at a given point is defined as:

$$\mathbf{B} = \begin{bmatrix} \frac{\partial N_1}{\partial x} & 0 & 0 & \cdots & \frac{\partial N_n}{\partial x} & 0 & 0 \\ 0 & \frac{\partial N_1}{\partial y} & 0 & \cdots & 0 & \frac{\partial N_n}{\partial y} & 0 \\ 0 & 0 & \frac{\partial N_1}{\partial z} & \cdots & 0 & 0 & \frac{\partial N_n}{\partial z} \\ \frac{\partial N_1}{\partial y} & \frac{\partial N_1}{\partial x} & 0 & \cdots & \frac{\partial N_n}{\partial y} & \frac{\partial N_n}{\partial x} & 0 \\ 0 & \frac{\partial N_1}{\partial z} & \frac{\partial N_1}{\partial y} & \cdots & 0 & \frac{\partial N_n}{\partial z} & \frac{\partial N_n}{\partial y} \\ \frac{\partial N_1}{\partial z} & 0 & \frac{\partial N_1}{\partial x} & \cdots & \frac{\partial N_n}{\partial z} & 0 & \frac{\partial N_n}{\partial x} \end{bmatrix}, \tag{A.3}$$

where N_i are the NURBS basis functions, and n is the number of non-zero basis functions at the evaluation point. The matrix $\mathbf{B}$ has dimensions $6 \times 3n$, corresponding to the six strain components in three dimensions and the $3n$ displacement degrees of freedom. For a spline volume of polynomial degrees p, q, and r, the number of non-zero basis functions is $n = (p+1)(q+1)(r+1)$.

Traction Transformation Matrix in 3D: To compute the traction vector $\boldsymbol{t} = \boldsymbol{\sigma} \cdot \mathbf{n}$ from the stress vector $\tilde{\boldsymbol{\sigma}}$ expressed in Voigt notation in three dimensions, we define a transformation matrix $\hat{\mathbf{N}} \in \mathbb{R}^{3\times 6}$ as follows:

$$\tilde{\boldsymbol{\sigma}} = \begin{bmatrix} \sigma_{xx} \\ \sigma_{yy} \\ \sigma_{zz} \\ \sigma_{xy} \\ \sigma_{yz} \\ \sigma_{xz} \end{bmatrix}, \quad \mathbf{n} = \begin{bmatrix} n_x \\ n_y \\ n_z \end{bmatrix}, \quad \boldsymbol{t} = \hat{\mathbf{N}}\,\tilde{\boldsymbol{\sigma}}.$$

The matrix $\hat{\mathbf{N}}$ is defined as

$$\hat{\mathbf{N}} = \begin{bmatrix} n_x & 0 & 0 & n_y & 0 & n_z \\ 0 & n_y & 0 & n_x & n_z & 0 \\ 0 & 0 & n_z & 0 & n_y & n_x \end{bmatrix}.$$

Appendix B. Displacements of Plane Strain Thick Cylinder

This section provides the analytical derivation of the radial displacement for a plane strain cylinder having internal and external radii R_i and R_o, respectively. The derivation is based on the stress fields presented in [Boresi and Schmidt, 2002]. In the case of plane strain ($\epsilon_{zz} = 0$), under the assumption that the cylinder is subject to an internal pressure p_i and an external pressure p_o, the stress fields are given by:

$$\sigma_{\theta\theta} = \frac{p_i R_i^2 - p_o R_o^2}{R_o^2 - R_i^2} - \frac{R_i^2 R_o^2 \left(p_o - p_i\right)}{r^2 \left(R_o^2 - R_i^2\right)} \tag{B.1}$$

$$\sigma_{rr} = \frac{p_i R_i^2 - p_o R_o^2}{R_o^2 - R_i^2} + \frac{R_i^2 R_o^2 \left(p_o - p_i\right)}{r^2 \left(R_o^2 - R_i^2\right)} \tag{B.2}$$

For plane strain conditions, the axial stress is given by:

$$\sigma_{zz} = \nu \left(\sigma_{rr} + \sigma_{\theta\theta}\right) \tag{B.3}$$

The tangential strain is given by:

$$\epsilon_{\theta\theta} = \frac{1}{E} \left[\sigma_{\theta\theta} - \nu \left(\sigma_{rr} + \sigma_{zz}\right)\right] \tag{B.4}$$

The following relation for the radial displacement holds:

$$\epsilon_{\theta\theta} = \frac{u_r}{r} \tag{B.5}$$

Substituting Eq.B.4 into Eq.B.5 yields:

$$u_r^{\text{plain strain}} = \frac{r\,(1+\nu)}{E\,(R_o^2 - R_i^2)} \left[(1-2\nu)\left(p_i R_i^2 - p_o R_o^2\right) + \frac{R_o^2 R_i^2}{r^2}\,(p_i - p_o) \right] \tag{B.6}$$

Appendix C. Control Points and Weights for the Third Case Study

Table C.3 lists the control points $\mathbf{P}_i = (x, y, z)$ and their corresponding weights used in defining the NURBS geometry for the dome with an oculus in the third case study. Figure C.23 illustrates the control polygon, where the control points are numbered for clarity.

Table C.3. Control points $\mathbf{P}_i = (x, y, z)$ and corresponding weights for the dome surface.

Point	x (m)	y (m)	z (m)	Weight
$\mathbf{P}_1$	15.00	0.00	0.00	1.0000
$\mathbf{P}_2$	20.00	0.00	0.00	1.0000
$\mathbf{P}_3$	25.00	0.00	0.00	1.0000
$\mathbf{P}_4$	15.00	15.00	0.00	0.7071
$\mathbf{P}_5$	20.00	20.00	0.00	0.7071
$\mathbf{P}_6$	25.00	25.00	0.00	0.7071
$\mathbf{P}_7$	0.00	15.00	0.00	1.0000
$\mathbf{P}_8$	0.00	20.00	0.00	1.0000
$\mathbf{P}_9$	0.00	25.00	0.00	1.0000
$\mathbf{P}_{10}$	15.00	0.00	14.4338	0.8070
$\mathbf{P}_{11}$	20.00	0.00	16.3894	0.8070
$\mathbf{P}_{12}$	25.00	0.00	18.3450	0.7669
$\mathbf{P}_{13}$	15.00	15.00	14.4338	0.5706
$\mathbf{P}_{14}$	20.00	20.00	16.3894	0.5706
$\mathbf{P}_{15}$	25.00	25.00	18.3450	0.5423
$\mathbf{P}_{16}$	0.00	15.00	14.4338	0.8070
$\mathbf{P}_{17}$	0.00	20.00	16.3894	0.8070
$\mathbf{P}_{18}$	0.00	25.00	18.3450	0.7669
$\mathbf{P}_{19}$	7.50	0.00	21.6506	0.8683
$\mathbf{P}_{20}$	7.50	0.00	22.7496	0.8683
$\mathbf{P}_{21}$	7.50	0.00	23.8485	0.9048
$\mathbf{P}_{22}$	7.50	7.50	21.6506	0.6140
$\mathbf{P}_{23}$	7.50	7.50	22.7496	0.6140
$\mathbf{P}_{24}$	7.50	7.50	23.8485	0.6398
$\mathbf{P}_{25}$	0.00	7.50	21.6506	0.8683
$\mathbf{P}_{26}$	0.00	7.50	22.7496	0.8683
$\mathbf{P}_{27}$	0.00	7.50	23.8485	0.9048

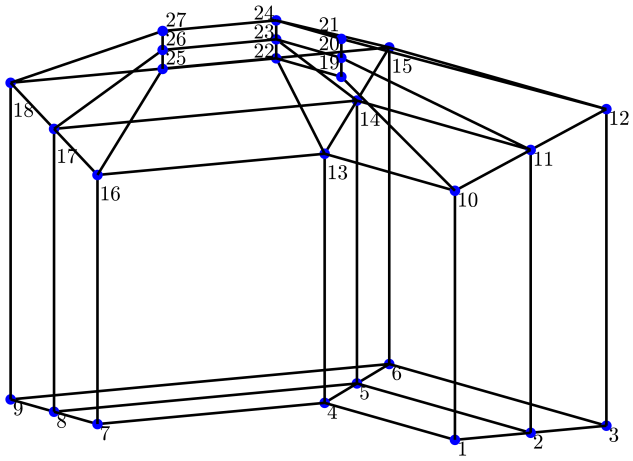

Fig. C.23. Control polygon of the dome geometry with numbered control points for the third case study.

Acknowledgment

A. Marzok acknowledges the support of Neubauer for establishing the Computational Solid Mechanics Research Group at the Technion. A. Marzok would also like to thank the Israeli Council for Higher Education for their generous support through the MAOF Fellowship. E. Shakur acknowledges the support of the Israel Science Foundation, grant number 2594/21.

Conflict of interest

The authors declare no conflict of interest.

References

Bailey, C., Cross, M., 1995. A finite volume procedure to solve elastic solid mechanics problems in three dimensions on an unstructured mesh. International Journal for Numerical Methods in Engineering 38, 1757–1776.

Boresi, A.P., Schmidt, R.J., 2002. Advanced mechanics of materials. John Wiley & Sons.

Cardiff, P., Demirdžić, I., 2021. Thirty years of the finite volume method for solid mechanics. Archives of Computational Methods in Engineering 28, 3721–3780.

Cardiff, P., Demirdžić, I., 2021. Thirty years of the finite volume method for solid mechanics. Archives of Computational Methods in Engineering 28, 3721–3780.

Cardiff, P., Tuković, Z., Jasak, H., Ivanković, A., 2016. A block-coupled finite volume methodology for linear elasticity and unstructured meshes. Computers & Structures 175, 100–122.

Costa, R., Nóbrega, J.M., Clain, S., Machado, G.J., 2021. Efficient very high-order accurate polyhedral mesh finite volume scheme for 3d conjugate heat transfer problems in curved domains. Journal of Computational Physics 445, 110604.

Costa, R., Nóbrega, J.M., Clain, S., Machado, G.J., Loubère, R., 2019. Very high-order accurate finite volume scheme for the convection-diffusion equation with general boundary conditions on arbitrary curved boundaries. International Journal for Numerical Methods in Engineering 117, 188–220.

Cottrell, J.A., Hughes, T.J., Bazilevs, Y., 2009. Isogeometric analysis: toward integration of CAD and FEA. John Wiley & Sons.

Cottrell, J.A., Reali, A., Bazilevs, Y., Hughes, T.J., 2006. Isogeometric analysis of structural vibrations. Computer methods in applied mechanics and engineering 195, 5257–5296.

Demirdžić, I., Martinović, D., 1993. Finite volume method for thermo-elasto-plastic stress analysis. Computer methods in applied mechanics and engineering 109, 331–349.

Demirdzic, I., Martinovic, P., Ivankovic, A., 1988. Numerical simulation of thermal deformation in welded workpiece. Zavarivanje 31, 209–219.

Demirdžić, I., Muzaferija, S., 1995. Numerical method for coupled fluid flow, heat transfer and stress analysis using unstructured moving meshes with cells of arbitrary topology. Computer Methods in Applied Mechanics and Engineering 125, 235–255.

Fryer, Y.D., Bailey, C., Cross, M., Lai, C.H., 1991. A control volume procedure for solving the elastic stress-strain equations on an unstructured mesh. Applied Mathematical Modelling 15, 639–645.

Gomez, H., Hughes, T.J., Nogueira, X., Calo, V.M., 2010. Isogeometric analysis of the isothermal navier–stokes–korteweg equations. Computer Methods in Applied Mechanics and Engineering 199, 1828–1840.

Gould, P.L., Feng, Y., 1994. Introduction to linear elasticity. volume 2. Springer.

Hughes, T.J., Cottrell, J.A., Bazilevs, Y., 2005. Isogeometric analysis: Cad, finite elements, nurbs, exact geometry and mesh refinement. Computer methods in applied mechanics and engineering 194, 4135–4195.

Idelsohn, S.R., Onate, E., 1994. Finite volumes and finite elements: two 'good friends'. International journal for numerical methods in engineering 37, 3323–3341.

Jasak, H., Weller, H.G., 2000. Application of the finite volume method and unstructured meshes to linear elasticity. International Journal for Numerical Methods in Engineering 48, 267–287.

Jiao, Z., Heblekar, T., Wang, G., Xu, R., Chen, W., Reddy, J., 2023. Analysis of plane elasticity problems using the dual mesh control domain method. Computer Methods in Applied Mechanics and Engineering 416, 116342.

Kagan, P., Fischer, A., Bar-Yoseph, P.Z., 1998. New b-spline finite element approach for geometrical design and mechanical analysis. International Journal for Numerical Methods in Engineering 41, 435–458.

Kagan, P., Fischer, A., Bar-Yoseph, P.Z., 2003. Mechanically based models: Adaptive refinement for B-spline finite element. International Journal for Numerical Methods in Engineering 57, 1145–1175.

McDonald, P.W., 1971. The computation of transonic flow through two-dimensional gas turbine cascades. volume 79825. American Society of Mechanical Engineers.

Nguyen, V.P., Anitescu, C., Bordas, S.P., Rabczuk, T., 2015. Isogeometric analysis: an overview and computer implementation aspects. Mathematics and Computers in Simulation 117, 89–116.

Onate, E., Cervera, M., Zienkiewicz, O.C., 1994. A finite volume format for structural mechanics. International Journal for Numerical Methods in Engineering 37, 181–201.

Papadakis, G., 2008. A novel pressure–velocity formulation and solution method for fluid–structure interaction problems. Journal of Computational Physics 227, 3383–3404.

Patankar, S.V., Spalding, D.B., 1972. A calculation procedure for heat, mass and momentum transfer in three-dimensional parabolic flows. International Journal of Heat and Mass Transfer 15, 1787–1806.

Piegl, L., Tiller, W., 1995. The NURBS Book. Springer.

Schäfer, M., Teschauer, I., 2001. Numerical simulation of coupled fluid–solid problems. Computer Methods in Applied Mechanics and Engineering 190, 3645–3667.

Sevilla, R., Giacomini, M., Huerta, A., 2019. A locking-free face-centred finite volume (fcfv) method for linear elastostatics. Computers & Structures 212, 43–57.

Shakour, E., Amir, O., 2021. Topology optimization with precise evolving boundaries based on iga and untrimming techniques. Computer Methods in Applied Mechanics and Engineering 374, 113564.

Shakur, E., Marzok, A., 2025. Isogeometric finite volume method for heat transfer simulations on curved spline-based geometries. Engineering with Computers , 1–25.

Suliman, R., Oxtoby, O.F., Malan, A.G., Kok, S., 2014. An enhanced finite volume method to model 2d linear elastic structures. Applied Mathematical Modelling 38, 2265–2279.

Vaz Jr, M., Muñoz-Rojas, P.A., Filippini, G., 2009. On the accuracy of nodal stress computation in plane elasticity using finite volumes and finite elements. Computers & Structures 87, 1044–1057.

Vinokur, M., 1989. An analysis of finite-difference and finite-volume formulations of conservation laws. Journal of computational physics 81, 1–52.

Wang, W.F., Mei, M., Wang, Z.Q., Zhou, Z.F., Wu, W.T., 2024. Compressible fsi of elastic spikes for drag reduction under hypersonic flow. International Journal of Mechanical Sciences 272, 109282.

Wang, Y., Wang, Z., Xia, Z., Poh, L.H., 2018. Structural design optimization using isogeometric analysis: a comprehensive review. Computer Modeling in Engineering & Sciences 117, 455–507.

Wenke, P., Wheel, M., 2003. A finite volume method for solid mechanics incorporating rotational degrees of freedom. Computers & Structures 81, 321–329.

Xuan, L., Yan, C., Gong, J., Li, C., Li, H., 2025. A penalty-based cell vertex finite volume method for two-dimensional contact problems. Computational Mechanics 75, 97–112.

Yang, X., Guo, N., Yang, Z., 2024a. A finite-volume implementation of the phase-field model for brittle fracture with adaptive mesh refinement. Computers and Geotechnics 165, 105921.

Yang, X., Li, B., Li, Y., Yang, B., Zhou, K., 2024b. A finite volume–based thermo-fluid-mechanical model of the lpbf process. International Journal of Mechanical Sciences 284, 109759.

Zienkiewicz, O.C., Taylor, R.L., Zhu, J.Z., 2013. The Finite Element Method: Its Basis and Fundamentals. 7 ed., Butterworth-Heinemann – Elsevier.